Air Force Institute of Technology

AFIT Scholar

3-26-2015

Photoluminescence and Optically Stimulated Luminescence Studies of LiAlO2 and LiGaO2 Crystals

Ian P. Ferguson

Follow this and additional works at: https://scholar.afit.edu/etd

PHOTOLUMINESCENCE AND OPTICALLY STIMULATED LUMINESCENCE STUDIES OF LiAlO$_2$ AND LiGaO$_2$ CRYSTALS

THESIS

Ian P. Ferguson, Second Lieutenant, USAF

AFIT-ENP-MS-15-M-106

DEPARTMENT OF THE AIR FORCE
AIR UNIVERSITY

AIR FORCE INSTITUTE OF TECHNOLOGY

Wright-Patterson Air Force Base, Ohio

PHOTOLUMINESCENCE AND OPTICALLY STIMULATED LUMINESCENCE

STUDIES OF LiAlO$_2$ AND LiGaO$_2$ CRYSTALS

THESIS

Presented to the Faculty

Department of Engineering Physics

Graduate School of Engineering and Management

Air Force Institute of Technology

Air University

Air Education and Training Command

in Partial Fulfillment of the Requirements for the

Degree of Master of Science in Applied Physics

Ian P. Ferguson, B.S.

Second Lieutenant, USAF

26 March 2015

PHOTOLUMINESCENCE AND OPTICALLY STIMULATED LUMINESCENCE

STUDIES OF LiAlO$_2$ AND LiGaO$_2$ CRYSTALS

THESIS

Ian P. Ferguson, B.S.
Second Lieutenant, USAF

Committee Membership:

Dr. Nancy C. Giles
Chair

Dr. Larry E. Halliburton
Member

Maj Eric M. Golden, PhD
Member

AFIT-ENP-MS-15-M-106

Abstract

Copper diffusion in $LiAlO_2$ creates large photoluminescence (PL) and optically stimulated luminescence (OSL) signals that are not present in as-grown samples. This enhancement in emission has applications in the development of sensitive and versatile radiation detectors. The main PL band peaks at 3.45 eV (359 nm) and is excited by a band peaking at 4.54 eV (273 nm). After x-ray irradiation, OSL results from 425-500 nm continuous wave light. An optical absorption band in the same region decays during optical stimulation. Analysis of the wavelength dependence of the OSL emitted light reveals a band that is similar in peak location and width to the PL band suggesting that they occur at the same copper defect. The defects causing this optical behavior were identified using electron paramagnetic resonance (EPR) spectroscopy. During x-ray irradiation, Cu^+ ions trap holes to become Cu^{2+} ions while Fe^{2+} ions trap electrons to become Fe^+ ions. As a result of optical stimulation, released electrons recombine with holes at the Cu^{2+} ion sites. Copper was also diffused into $LiGaO_2$. A large PL signal was observed to peak at 2.33 eV (532 nm) when excited by 3.50 eV (354 nm) light. This PL signal in $LiGaO_2$ is assigned to Cu^+ ions substituting for Li^+ ions.

iv

For the fellows of the Miami Valley Philosophical and Lifting Society

Acknowledgements

I would like to thank my advisor, Dr. Nancy Giles, for giving me the opportunity to work in this wonderful field of research, Capt M. Shamaun Holston for teaching me all of the experimental techniques that I used in this thesis and for the conversations that made every day in the lab enjoyable, Maj Eric Golden for taking the time to answer all of my questions, even if it was the same question repeated multiple times, Dr. Larry Halliburton for teaching me a healthy sense of skepticism and for all of our conversations (especially the more historical and philosophical ones), Mr. Greg Smith and Mr. Mike Ranft for always bailing me out of tricky situations with the lab equipment, and my parents and brother for their love and support.

2nd Lieutenant Ian P. Ferguson

Table of Contents

List of Figures

List of Tables

PHOTOLUMINESCENCE AND OPTICALLY STIMULATED LUMINESCENCE STUDIES OF LiAlO$_2$ AND LiGaO$_2$ CRYSTALS

I. Introduction

1.1 Motivation

PHOTOLUMINESCENCE (PL) and optically stimulated luminescence (OSL) are important characterization techniques that can help identify defects in a wide range of materials. An understanding of these defects within a material that exhibits OSL can be useful for radiation dosimetry in a variety of applications that are relevant to the Department of Defense (DoD). OSL dosimetry can be divided into three main areas: retrospective, personal, and environmental; all of which are pertinent to the DoD [1]. In terms of retrospective dosimetry, the DoD could apply OSL to assess the dose imparted on an area due to a nuclear or radiological event, thus providing the ability to respond to future attacks and better understand attacks and tests from the past. In terms of personal dosimetry, OSL dosimeters could potentially replace thermoluminescence dosimeters (TLDs) which are widely used by individuals conducting research and maintaining nuclear weapons (OSL dosimeters are a promising alternative to TLDs because they do not have to be heated to be read). Finally, OSL has the potential for environmental dosimetry, particularly for the DoD's assets in space where accurate dosage measurements are necessary to ensure the proper functioning of electronics aboard satellites.

The crystals chosen for this study are of interest because they contain lithium, unlike Al$_2$O$_3$:C, the most commonly used OSL dosimeter [2]. The large neutron

cross section of lithium-6 makes enriched $LiAlO_2$ and $LiGaO_2$ good candidates for detecting thermal neutrons [3]. Lithium compounds can also be used for tritium breeding which makes them potentially useful in nuclear fusion reactions [4]. Copper was chosen as the material to diffuse into the crystals because it has been established that copper-doping can improve OSL dosimetry performance [5].

1.2 Point Defects

Any interruption in the periodic structure of a crystal is known as a defect. These interruptions can occur at a single point, along a line, or across a plane within the crystal lattice. The effects reported in this thesis are the result of point defects, therefore only point defects are discussed below. Point defects can be described as intrinsic, meaning the defect involved is an ion that is native to the crystal (or contained in the crystal's chemical formula), or extrinsic, meaning an impurity that is not native to the crystal. Furthermore, defects can be described as substitutional, meaning the defect occurs at a normal atomic site within the crystal lattice, or interstitial meaning the ion or impurity occurs in between normal atomic sites. The specific names of the point defects according to these criteria are listed in table 1.

	intrinsic	extrinsic
interstitial	self interstitial	interstitial impurity
substitutional	vacancy or antisite	substitutional impurity

Table 1. Summary of the different types of point defects.

It should be noted that there are two point defects in the substitutional, intrinsic category. Vacancy, as the name suggests, refers to an absence of an ion that would ordinarily exist at a site within the lattice. Antisite refers to the substitution of an

ion with another ion that is part of the crystal's chemical composition.

An important property of crystals is their charge neutrality. In order to maintain charge neutrality, point defects must not modify the net charge of the crystal. For example, a lithium cation (Li^+) could substitute for a sodium cation (Na^+) in an NaCl crystal, but a calcium cation (Ca^{2+}) could not substitute for a sodium cation unless accompanied by another defect that compensates for the additional charge (a sodium vacancy would work in this situation). Two common examples of how charge neutrality can be maintained when intrinsic point defects occur are Schottky and Frenkel defects which are depicted in figure 1. In the Schottky defect, a cation vacancy is compensated with an anion vacancy. In the Frenkel defect, a self interstitial is compensated with a vacancy of that same ion [6].
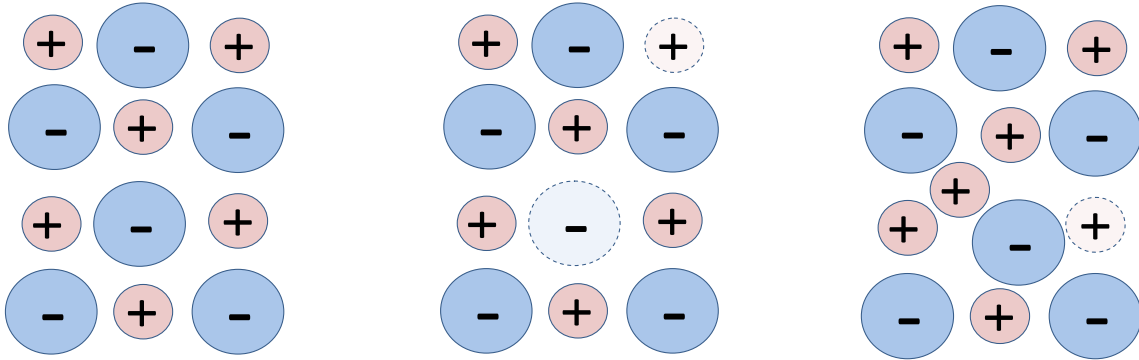
Figure 1. Examples of point defects in crystals with charge neutrality. The left figure represents a perfect crystal lattice. The center figure represents a Schottky defect. The right figure represents a Frenkel defect. Vacancies have dashed outlines.

Impurities can produce an alteration of the allowed energy levels within a crystal's band structure. The energy bands of a crystal arise because an electron in the crystal will experience a periodic potential function due to the periodic arrangement of the nuclei contained in that crystal. The solution to the Schrödinger wave equation for such a potential reveals that wave functions for the electrons in the crystal can either be localized around specific nuclei or they can be spread across the crystal lattice (delocalized). Electrons with the latter wave function are said to be in an energy

band. Within these bands, the energy levels of the available quantum states are so closely spaced that they are considered continuous. The energy separation between two specific bands, the conduction and valence bands, is known as the band gap of the crystal [6].

The spacing of the energy bands, and their locations with respect to the Fermi energy level (the highest energy level occupied by an electron at 0 K) vary depending on the type of material. In metals, the Fermi energy level falls in a delocalized conduction band. Therefore, metals contain electrons that are free to move throughout the crystal lattice at any temperature. The Fermi energy level of insulators and intrinsic semiconductors falls between the valence and conduction bands. In these materials, all the electrons are contained in the valence band at 0 K. The difference between insulators and intrinsic semiconductors lies in the spacing of the energy bands. Insulators have large band gap energies, so no appreciable amount of electrons are excited to the conduction band unless the material is heated to high temperatures. Intrinsic semiconductors have small band gap energies, so electrons can be excited to the conduction band at room temperature. Impurities, or other defects, can modify the band structure of materials by providing additional energy levels within the forbidden energy zone between the valence and conduction bands. The presence of these extra energy levels can produce a variety of different optical behaviors. In this study, copper defects produce PL and OSL in an insulator crystal.

1.3 Lithium Aluminate

$LiAlO_2$ has tetragonal symmetry, space group $P42_12$, with the following lattice constants: $a = 5.1687$ Å and $c = 6.2679$ Å. Every lithium ion and every aluminum ion has four oxygen nearest neighbors. In the lattice, every oxygen ion has two lithium and two aluminum nearest neighbors. Oxygen occupies one crystallographically distinct

4

site at the center of the tetrahedra formed by the lithium and aluminum ions [7]. The LiAlO$_2$ crystal structure is depicted in figure 2.
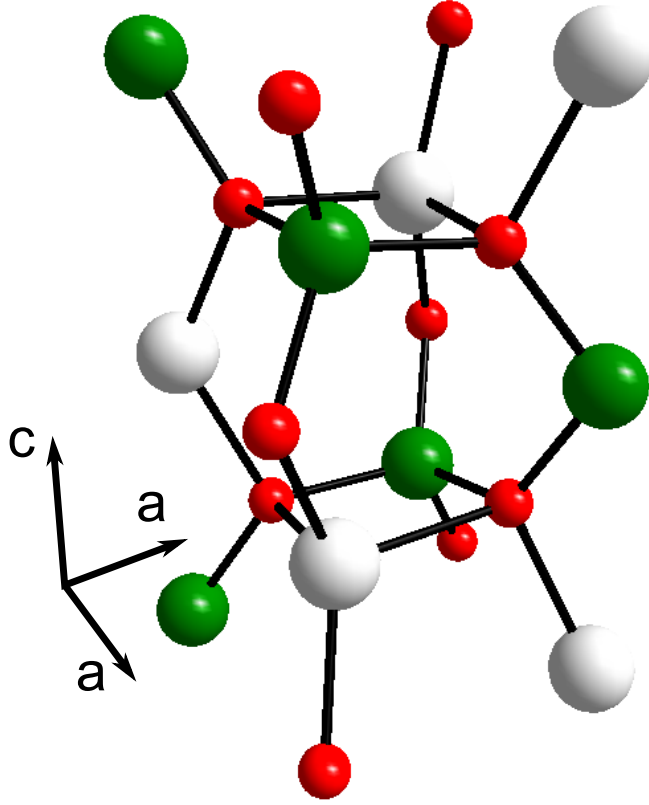
Figure 2. Representation of LiAlO$_2$ crystal using the Diamond software package from Crystal Impact. Lithium, aluminum, and oxygen ions are colored white, green, and red, respectively.

Research on LiAlO$_2$ expanded in the late 1990s after Xu et al. showed that LiAlO$_2$ could be used as a substrate material for GaN growth because of the small lattice mismatch between the two crystals [8]. Furthermore, the relatively low melting point and hardness of LiAlO$_2$ allow it to be etched from the GaN. Shortly thereafter, Chou et al. proposed making surface acoustic wave devices for frequency filters with LiAlO$_2$ because of its high acoustic velocities [9]. Recent work has shown that undoped LiAlO$_2$ is an effective OSL dosimeter [10], as well as LiAlO$_2$ doped with terbium [11] and manganese [12].

1.4 Lithium Gallate

LiGaO$_2$ has orthorhombic symmetry, space group $Pna2_1$, with the following lattice constants: $a = 5.402$ Å, $b = 6.372$ Å, and $c = 5.007$ Å. Every lithium ion and every gallium ion has four oxygen nearest neighbors, and every oxygen ion has two gallium and two lithium nearest neighbors. Oxygen occupies two crystallographically distinct sites [13]. The LiGaO$_2$ crystal structure is depicted in figure 3.
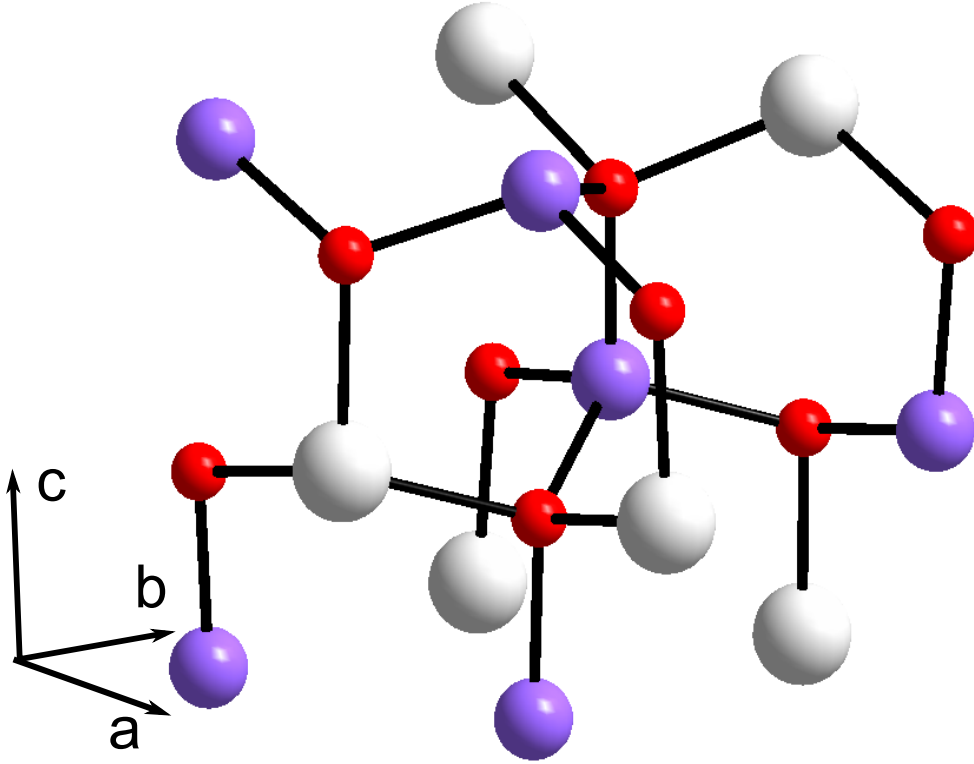
Figure 3. LiGaO$_2$ crystal using the Diamond software package from Crystal Impact. Lithium, gallium, and oxygen ions are colored white, purple, and red, respectively.

Like LiAlO$_2$, interest in LiGaO$_2$ grew once Kung et al. demonstrated that it could be used as a substrate for growing GaN films [14]. In addition to GaN, Johnson et al. successfully grew InGaN and AlGaN using LiGaO$_2$ substrates [15]. Recently, ZnO has also been grown on this substrate material [16]. Unlike LiAlO$_2$, extensive research has not been conducted concerning the feasibility of LiGaO$_2$ as an OSL dosimeter.

II. Photoluminescence

2.1 Background

L UMINESCENCE is the process by which an external energy source causes a material to emit light. There are several different potential sources of this external energy, including electrons, heat, electric fields, and chemical and biological processes. Photoluminescence, the form of luminescence caused by an external light source, was first observed by William Herschel in 1845 when he noticed that tonic water glows with a green tint when illuminated by bright sources of sunlight. This phenomenon is the result of incident light causing electrons within the molecules in the compound to move to an excited state. The excited electrons eventually relax to their ground state resulting in the emission of light. Photoluminescence can be divided into two categories: fluorescence, where the ground and excited electron orbitals have equal spin values, thus the excitation and emission occur relatively quickly (on the order of nanoseconds) and phosphorescence, where the ground and excited orbitals have different spin values and there is a longer time between the absorption and the emission (milliseconds to hours) [17].

The analysis of photoluminescence spectra is an effective means for determining the optical quality of a material and any defects that the material may contain. There are several advantages to photoluminescence studies: it is nondestructive to the material, it requires a small amount of material, it can be performed at room temperature (although there are some situations where lowering the temperature is necessary), and it is sensitive to very small defect concentrations in a crystal. Photoluminescence also has disadvantages: it cannot accurately determine the concentration of observed defects and it is difficult to identify the type of defect with photoluminescence alone (photoluminescence is more powerful when combined with other techniques such as

electron paramagnetic resonance) [18].

2.2 Configuration Coordinate Diagram and Stokes Shift

Shortly after Herschel's discovery, George Stokes noticed that the wavelength of the emitted light is longer than the wavelength of the absorbed light, a behavior known as a Stokes shift [17]. Stokes shifts can be explained by the configuration coordinate diagram which is illustrated in figure 4. When an electron is excited to a higher energy state, it changes the effective size of the ion in the crystal that contains the electron which, in turn, alters the equilibrium configuration of the surrounding ions in the crystal. Thus, the potential functions of the ground state configuration and excited state configurations do not align. Electron transitions occur over shorter time intervals than nuclear oscillations, so the separation and relative momentum of neighboring nuclei within the crystal can be considered constant during an electron transition. Electrons can transfer between any of the vibrational states within the ground and excited electronic states, but according to the Franck-Condon principle, the probability that the transition occurs is determined by the degree to which the wave functions overlap with one another, causing certain transitions to be favored. Typically, the wave functions that overlap the most correspond to different vibrational states within the electronic states. Once an electronic transition occurs, the electron relaxes to the lowest vibrational state in the excited electronic state before falling back to the ground electronic state. As a result the energy associated with the absorption transition is higher than the energy associated with the emission transition [19].

It is important to note that the absorption of a photon can lead to nonradiative recombinations as well as fluorescent radiative recombinations. In the event that the potential curves in the configuration coordinate diagram intersect with one another, an excited electron can decay back to the ground state by exclusively emitting

phonons, thus there are no photons emitted and fluorescence does not occur.
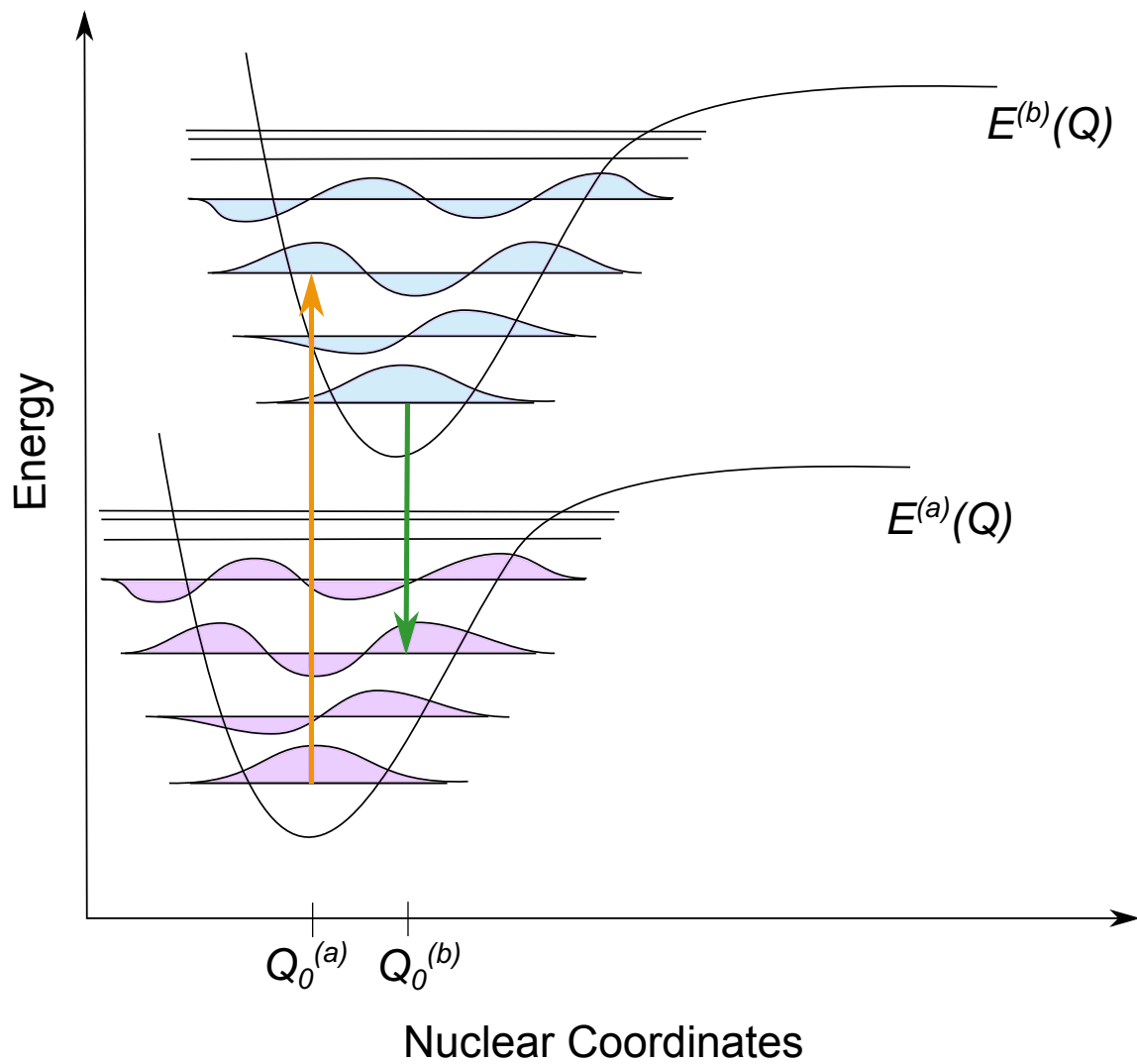
Figure 4. Configuration coordinate diagram illustrating Stokes shift and the Franck-Condon principle. The orange arrow represents the absorption transition and the green arrow represents the emission transition. The horizontal lines represent the energy levels of the vibrational states within the electronic states.

2.3 Shape of Photoluminescence Spectra

If the absorption represented by the orange arrow and the emission represented by the green arrow in figure 4 were the only possible transitions, photoluminescence absorption and emission spectra would appear as narrow lines at low temperature. Additional spectral structure arises, however, due to transitions from different vibrational states within the electronic states. A mathematical description of this spectral structure (assuming low temperature and simple harmonic oscillator electronic states) uses the dimensionless Huang-Rhys parameter, S:

$$S = \frac{1}{2}\frac{M\omega^2}{\hbar\omega}(Q_0^{(b)} - Q_0^{(a)})^2, \tag{1}$$

where M is the effective ionic mass, ω is the vibrational frequency of the oscillator, and $Q_0^{(a)}$ and $Q_0^{(b)}$ are the nuclear configuration coordinates of the bottom of the potential wells representing electronic states a and b respectively [20].

The Huang-Rhys factor, $F_m(0)$, is used to calculate the probability that a transition will occur from the ground electronic state to the m vibrational level within the excited electronic state:

$$F_m(0) = \frac{\exp(-S)S^m}{m!}, \tag{2}$$

which, in turn, leads to the absorption band shape function:

$$I_{ab}(E) = I_0 \sum_m \frac{\exp(-S)S^m}{m!}\delta(E_0 + m\hbar\omega - E). \tag{3}$$

The shape of absorption bands with different S values is displayed in figure 5. In the event that there is no displacement between the nuclear coordinates of the equilibrium position of the ground and excited states, $Q_0^{(a)} = Q_0^{(b)}$ and $S = 0$. The result is that all of the intensity of the absorption band is contained in the *zero phonon transition*

10
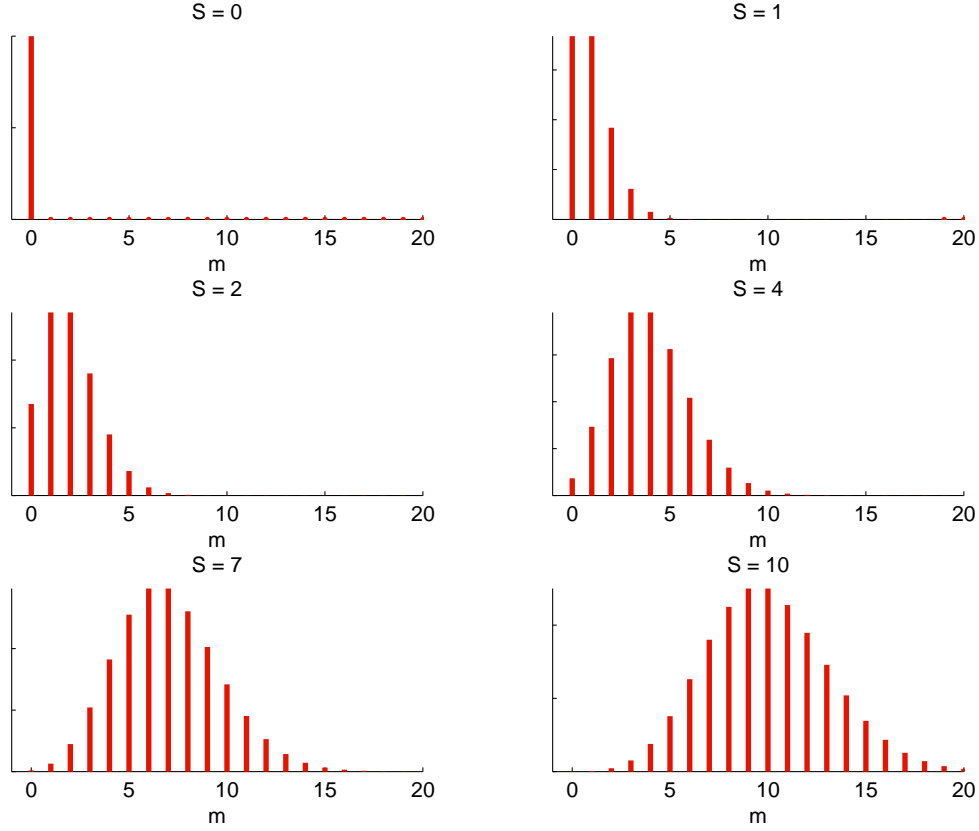
Figure 5. Absorption band shapes for varying Huang-Rhys parameter values at 0K.

where $m = 0$. As S increases, the total intensity of the absorption band remains the same, but it is shared between the zero phonon line and *vibrational sidebands* which occur at energy increments of $m\hbar\omega$ above the zero phonon line (thus the x axis of figure 5 is plotted in terms of m instead of E). As S increases to even higher values, the zero phonon line vanishes and all of the intensity is contained in vibrational sidebands. The absorption band also becomes more symmetric as S increases and approaches a Gaussian shape [20].

A similar probabilistic approach can be used to predict the emission spectrum. If both the ground and excited state potential functions were perfect parabolas, then the emission spectrum would simply be a reflection of the absorption spectrum across the zero phonon line. This is a somewhat accurate approximation, but is not perfect

11

because the potential functions are not identical. In most cases, the wave functions associated with excited electronic states will be more spread out than those in ground electronic states. One can think of this as the result of the displacement of the neighboring atoms in the crystal lattice when an electron is excited which allows the excited electron more space. One can also think of this in terms of the electron shells themselves; for example an electron from a Cu^+ ion in a $LiAlO_2$ crystal will be excited from a $3d$ shell to a $4s$ shell and $4s$ wave functions tend to be more dispersed than $3d$ wave functions. In either case, the result is an excitation band that is slightly narrower than the emission band.

III. Optically Stimulated Luminescence

3.1 Background

THE earliest evidence for optically stimulated luminescence (OSL) comes from Edmond Becquerel and Henri Becquerel who observed the phenomenon in zinc sulfide and calcium sulfide in 1843 and 1883, respectively. An understanding of OSL arrived with the discovery of quantum mechanics and, by the 1940s, a consensus about its underlying mechanics was reached [21]. OSL is similar to photoluminescence in the sense that luminescent emission is achieved by stimulating light; however, OSL is the result of the recombination of charges that were separated into metastable trapped states, not the excitation and relaxation of charges within one defect. Therefore, OSL differs from PL in that OSL requires a previous source of excitation and the stimulating light for OSL can be of longer or shorter wavelength than the emitted light, whereas the stimulating light for PL must be of shorter wavelength than the emitted light (see section 2.2).

OSL was first proposed as a personal dosimetry measurement technique in 1959, but was not widely employed because the known OSL materials contained shallow charge traps from which charge could be released by the thermal energy from storage at room temperature, an effect also known as *fading*. The interest in OSL for personal dosimetry has resurfaced in the last twenty years as the result of the discovery of materials with deeper charge traps. Another noteworthy application of OSL is in the field of archaeological and geological dating. Naturally occurring radioactive isotopes can separate charges in quartz sediments. Sunlight stimulates the recombination of these charges, so archaeologists and geologists can determine the length of time that a specimen has been buried based on the strength of the OSL signal [22]. OSL has also been demonstrated as a successful means for measuring radiation doses on spacecraft,

on patients receiving medical radiation treatment, and detecting potential weapons of mass destruction. For the purpose of this study, OSL is used in conjunction with other techniques to analyze defects contained in a crystal.

The basic process of OSL can be described in three stages: excitation, latency, and stimulation, which can be seen in figure 6. During the excitation phase, the crystal is exposed to an excitation source which promotes an electron to the conduction band and leaves a hole in the electron's place in the valence band. Typically, the excitation source is ionizing radiation in the form of γ-rays or x-rays. Once the excitation has occurred, the electron and hole can move freely in their respective bands until they become trapped at certain defect sites. The latency phase consists of trapped charges remaining in their metastable states. Depending on the depth of the potential wells associated with these states, the charges may be stimulated by room temperature thermal energy to recombine, or they may remain trapped indefinitely. The final step, stimulation, occurs when light with sufficient energy excites the electron out of its trap so that it can recombine with the hole producing the OSL light. Typically the photon must have sufficient energy to promote the electron from the trap to the conduction band in order to cause OSL.
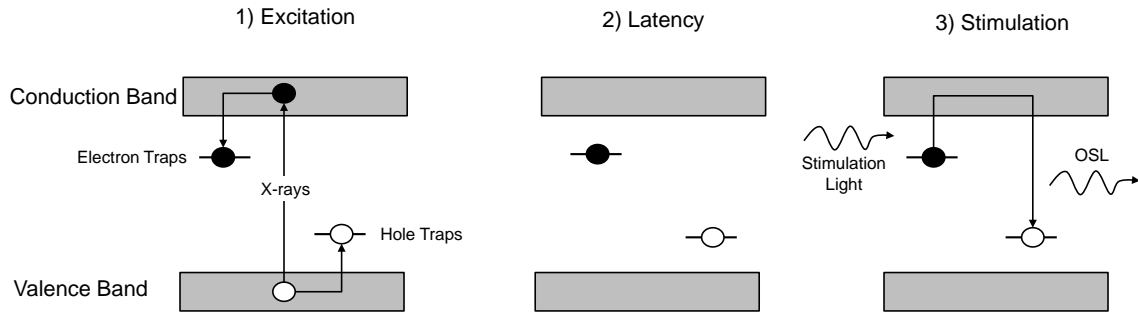

Figure 6. The phases of OSL. Black circles indicate electrons and white circles indicate holes. Grey areas indicate bands of accessible states. Horizontal lines indicate additional energy levels added by point defects. This figure is adapted from a similar figure in Yukihara and McKeever's research monograph [21].

3.2 Trapping and Recombination

In the ideal insulator or semiconductor crystal, an electron with sufficient energy can be promoted to the conduction band where it moves freely until it relaxes to the valence band. Point defects interrupt this free movement because they introduce electric fields that can interact with the electron. Electrons moving in the conduction band (and holes moving in the valence band) become trapped when they are attracted to such defects and occupy one of the bound energy states of that defect. These energy states can occur at any energy level between the valence band and the conduction band. During excitation, point defects with bound energy levels closer to the valence band are more likely to trap holes, so they are called hole traps, while those near the conduction band are more likely to trap electrons and are called electron traps (see figure 6). Some defects have energy levels in the middle region and have near equal probabilities of capturing electrons and holes. These are known as recombination centers because they can capture a hole then an electron or vice versa, causing a recombination.

3.3 Optical Stimulation

Optical stimulation, the final stage in the OSL process mentioned in section 3.1, occurs when incident light provides the energy to release charges from their trapped states. In the simplest scenario, photons with sufficient energy promote trapped electrons to the conduction band, then every electron recombines with a hole and releases light. Without the possibility of retrapping once the electron is promoted to the conduction band, the concentration of trapped charge n, will vary with time according to the differential equation:

$$\frac{dn}{dt} = -np,\tag{4}$$

where p is the probability that an incident photon will interact with the trapped charge. This leads to the following time dependence of the intensity of the OSL light:

$$I_{\text{OSL}}(t) \propto n_0 p e^{-pt}, \tag{5}$$

where n_0 is the concentration of trapped charges when the stimulation begins. For most materials that exhibit OSL, including the most common OSL dosimeter, Al_2O_3:C, p is proportional to the incident photon flux of the stimulating light, ϕ:

$$p = \phi\sigma, \tag{6}$$

where σ represents the photoionization cross section of the defect involved with trapping the charge. Although less common, not all materials obey this linear relationship. In the case of NaCl for example, p is more closely proportional to $\sqrt{\phi}$ [21].

A theoretical description of the photoionization cross section, σ, is difficult because the shapes of the potential wells associated with point defects are not well defined, thus the wave functions of trapped electrons are not well defined. The problem is further obscured because not all OSL emission is the result of electrons promoted directly to the conduction band (some trapped electrons are excited to more shallow traps and are then released by thermal energy). Grimmeiss and Ledebo have formulated the most accurate approximation of the photoionization cross section by assuming a delta potential function for the charge traps [23]:

$$\sigma(h\nu) = \frac{(h\nu - E_I)^{3/2}}{h\nu[h\nu + E_I(m_0/m^* - 1)^2]}. \tag{7}$$

In this equation, E_I is the energy separation of the point defect's energy level and the conduction band, m_0 is the mass of a free electron, and m^* is the effective mass

of an electron moving in the conduction band.

Along with some other factors, the photoionization cross section can be used to formulate theoretical models of the OSL processes. The simplest model involves one discrete electron trap energy level, one discrete recombination center level, and the valence and conduction bands as shown in figure 7 (the caption for figure 7 also contains the description of the terms used in the differential equations below).
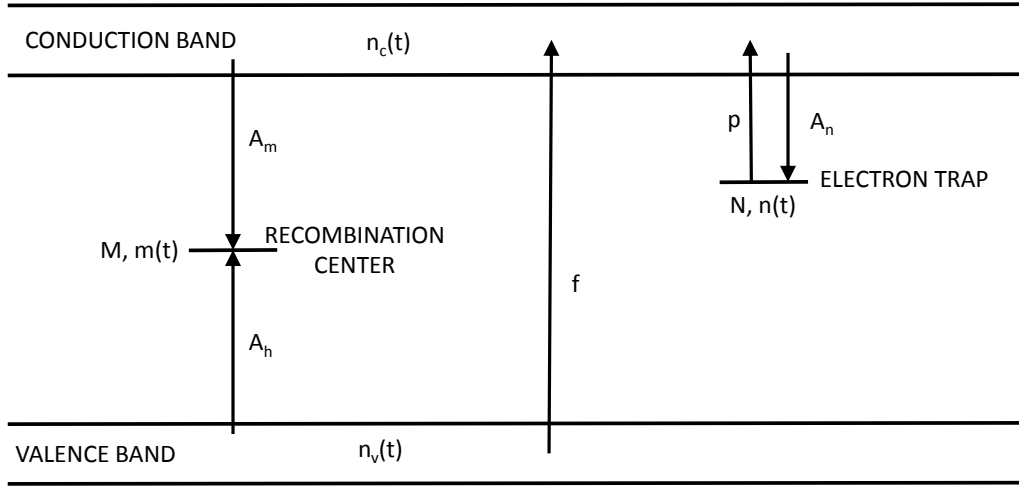
Figure 7. Diagram of the one trap one recombination center (OTOR) model. M **and** N **represent the total concentration of recombination sites and trap sites.** $m(t)$ **and** $n(t)$ **represent the concentration of trapped holes and electrons.** $n_c(t)$ **and** $n_v(t)$ **represent the concentration electrons in the conduction band and holes in the valence band.** A_m **represents the probability of electrons recombining from the conduction band.** A_h **represents the probability that holes will be trapped by the recombination center.** A_n **represents the probability that conduction band electrons will be trapped by the electron trap.** p **is the probability of detrapping term described in equation 6.** f **describes the concentration of charge per unit time that is excited by a radiation source.**

This model is aptly named the one-trap, one-recombination model, or the OTOR model. Using terms for the concentration of total trapping and recombination sites and terms for the probability of electron trapping and recombination from the conduction and hole trapping from the valence band, Yukihara and McKeever assign the

following rate equations for the OTOR model [21]:

$$\frac{dn(t)}{dt} = [N - n(t)]A_n n_c(t) - n(t)p \tag{8}$$

$$\frac{dm(t)}{dt} = [M - m(t)]A_h n_v(t) - m(t)A_m n_c(t), \tag{9}$$

which describe the concentration of trapped electrons at the electron trap, $n(t)$, and trapped holes at the recombination center, $m(t)$, along with the following rate equations that describe the concentration of electrons in the conduction band, $n_c(t)$, and the concentration of holes in the valence band, $n_v(t)$:

$$\frac{dn_c(t)}{dt} = f - \frac{dn(t)}{dt} - m(t)A_m n_c(t) \tag{10}$$

$$\frac{dn_v(t)}{dt} = f - [M - m(t)]A_h n_v(t). \tag{11}$$

By applying the condition that the OSL process moves sufficiently slow, so that the concentration of electrons in the conduction band and the concentration of holes in the valence band are both small, slowly changing numbers (i.e. $dn_c(t)/dt = 0$ and $dn_v(t)/dt = 0$), this system of differential equations can be simplified. Equation 9 becomes:

$$\frac{dm(t)}{dt} = f - m(t)A_m n_c(t), \tag{12}$$

where

$$n_c(t) = \frac{f + n(t)p}{[N - n(t)]A_n + m(t)A_m}. \tag{13}$$

The general solution to this simplified set of differential equations was obtained numerically using the built-in Runge-Kutta 4 algorithm for MATLAB software, the results of which are shown below. Figure 8 demonstrates how the shape of the OSL signal curve becomes steeper when there is a greater initial concentration of trapped holes at the recombination site. Although both of the curves in this figure appear to

be exponential, they are more accurately described by what Chen and Leung refer to as a stretched exponential $(\exp(-(t/\tau)^{\beta}))$, where the τ and β terms vary among materials [24]. More complicated OSL systems can be modeled by adding additional terms to the differential equations for additional electron and hole traps.
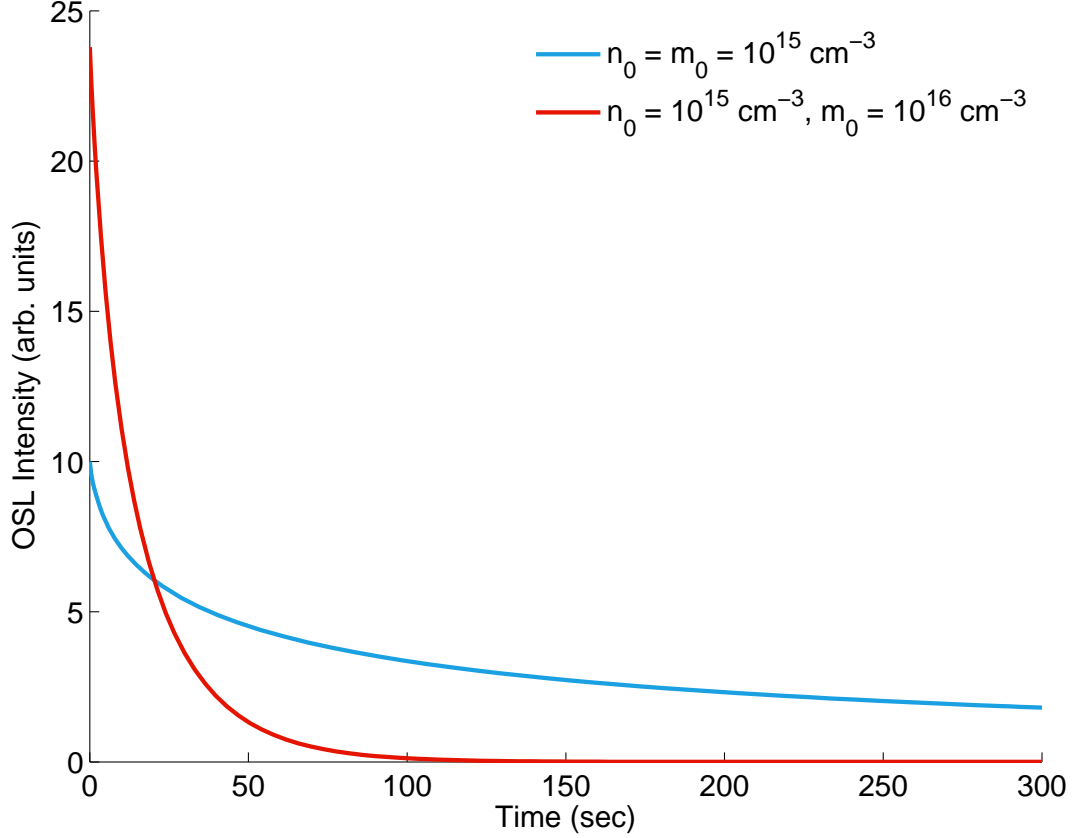
Figure 8. Numerical solution for equations 8 and 13, with different initial conditions, using a Runge-Kutta 5 algorithm. Parameters used in the solution include: $f = 0$ (no irradiation in process), $A_n = A_m = 10^{-8} \text{cm}^3/\text{s}$, $N = 10^{15} \text{cm}^{-3}$, $p = 0.1/\text{s}$.

3.4   Temperature Dependence

Although it will not be discussed in much depth in this thesis, temperature has noteworthy effects on OSL intensity. The first such effect, shallow trap competition, causes OSL signal intensity to increase with temperature if shallow electron traps are present in addition to the deep trap that is stimulated by the external light. At low

temperatures, electrons that are stimulated out of the deep traps can be retrapped by the shallow traps instead of recombining with trapped holes. As temperature increases, the shallow traps trap fewer electrons which allows more electrons to recombine and produce the OSL signal.

Above a certain threshold temperature, however, the OSL signal intensity declines due to an effect called thermal quenching. Thermal quenching occurs for two reasons: first, as temperature increases, electrons tend to occupy higher vibrational states which can lead to a greater number of nonradiative relaxations (see section 2.2), thus fewer radiative relaxations and a smaller OSL signal. Also at the threshold quenching temperature, a significant number of holes can be released from the recombination sites leaving fewer electron-hole pairs available to contribute to the OSL signal intensity.

3.5 Stimulation Modalities

Stimulation modality refers to the type of light used to release the trapped charges in the OSL process. The simplest stimulation modality, known as continuous wave OSL (abreviated CW-OSL), involves stimulation light of constant intensity. Besides the advantage of its simplicity in instrumentation, CW-OSL is also advantageous because it is the easiest modality to model theoretically, making the CW-OSL signals the simplest to interpret. The main disadvantage associated with CW-OSL is that the stimulating light can interfere with the OSL signal, therefore, the experimenter must make sure that the stimulating light wavelength band and the emitted light wavelength band do not overlap with one another [1].

In order to avoid this problem of overlapping stimulation and emission bands, researchers devised pulsed OSL (POSL). Pulsed OSL uses a short pulse of stimulating light to release charges from their traps. Most POSL systems also include some sort

of optical filter that protects the photomultiplier from over saturation during the pulse and is removed after the pulse so that the system can detect small amounts of emitted light. The drawbacks of POSL include the instrumental complications of creating pulsed light that is synchronized with a moving optical filter, as well as being limited to materials with emission lifetimes longer than the duration of the light pulse.

A third stimulation modality, known as linear modulation OSL (LM-OSL), involves gradually increasing the intensity of the stimulation light. Typically this is accomplished with an LED stimulation source where current to the LEDs is increased linearly with respect to time. Although this adds a complication to the OSL system, the advantage of LM-OSL is that it produces a signal from which multiple traps can easily be distinguished visually. While multiple traps in a CW-OSL signal produce a stretched exponential that looks similar to the stretched exponential of one trap, LM-OSL signals often produce signals with peaks for each of the traps. The additional complications to the system to produce LM-OSL are not always necessary because mathematical transformations of CW-OSL, called pseudo-LM-OSL, curves can imitate LM-OSL to make different traps more evident from the data [25].

IV. Experimental Techniques

4.1 Instrumentation

A detailed study of photoluminescence and optically stimulated luminescence requires a spectrofluorometer. For the present investigation, a Jobin Yvon Fluorolog-3-22 spectrofluorometer was used (in this thesis, the terms "spectrofluorometer" and "Fluorolog" are used interchangeably). The first type of measurement that can be taken with the Fluorolog is a photoluminescence emission (PL) scan. This involves exciting the sample with light of a specific wavelength and monitoring the intensity of the light emitted from the sample over a series of wavelengths. The second type of measurement is the photoluminescence excitation (PLE) scan. Here, the intensity of the emitted light of a specific longer wavelength is monitored as the sample is excited with light over a series of shorter wavelengths. The third type of measurement is optically stimulated luminescence (OSL) where the sample is excited with a specific wavelength and the emitted intensity is monitored at a specific shorter wavelength as a function of time.

There are multiple ways in which spectrofluorometers produce excitation light and monitor emission light of specific wavelengths. The Fluorolog, shown in figure 9, uses an excitation or entrance double monochromator to provide specific excitation wavelengths to the sample chamber from a xenon arc lamp. A second double monochromator known as the exit or emission monochromator filters the light emitted from the sample chamber before it enters a detector.

The ideal spectrofluorometer would produce excitation light with a constant photon flux output across all wavelengths, it would be equally sensitive to emission light of all wavelengths, and it would detect no stray light (i.e., light that is not the result of luminescence). The components of the Fluorolog are designed to resemble the
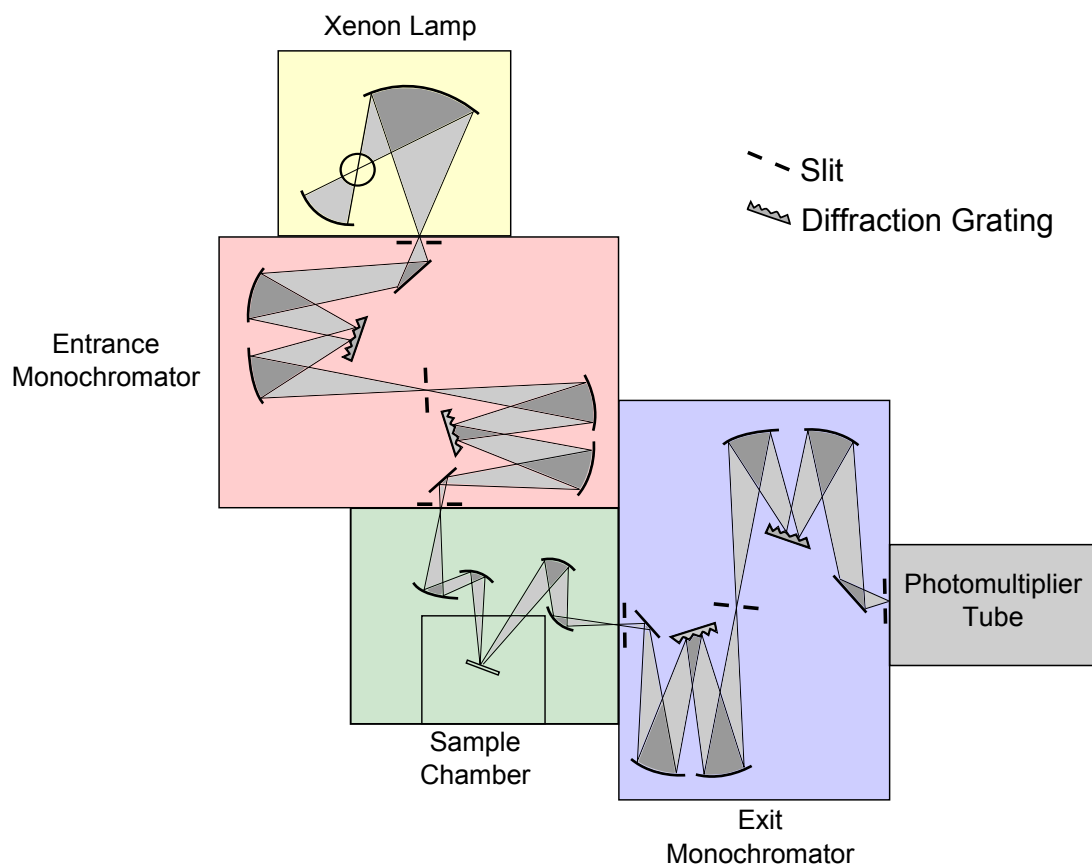
Figure 9. Top view of the Fluorolog-3-22 spectrofluorometer.

ideal spectrofluorometer as closely as possible. The Fluorolog uses a 450 W xenon arc lamp which provides a relatively smooth power curve in the 250 to 700 nm range. This is the result of the great deal of light from the xenon lamp that is produced from the recombination of ionized xenon and free electrons that are not restricted to specific energy levels. Xenon does, however, also emit some light from excited electron states which results in sharper spectral features between 450 and 500 nm and above 700 nm. Light detection in the Fluorolog is accomplished with a Hamamatsu R928 photomultiplier tube. This tube is most sensitive in the visible region of the spectrum, and loses sensitivity below 300 nm and above 700 nm. To reduce stray light, both the entrance and the exit monochromators are equipped with double diffraction gratings and multiple variable slits which are intended to only allow light

of the desired wavelength to pass through.

4.2 Spectrofluorometer Calibration

Despite the intentional design features mentioned in the previous section that optimize the Fluorolog's performance, it is still not the ideal spectrofluorometer, therefore calibration is required for the instrument. The first kind of calibration is spectral calibration, or determination that the spectrofluorometer is reading the correct wavelengths for the emitted light and providing the correct wavelengths of excitation light (getting the right x values for a PL or PLE plot). The other kind of calibration is intensity calibration, namely correcting for the features of the system that distort the relative intensity measurements (getting the right y values for a PL or PLE plot).

Spectral calibration for the spectrofluorometer's exit monochromator was accomplished using an Ocean Optics HG-1 mercury-argon calibration lamp. To measure the lamp's spectrum, the beam from the xenon excitation lamp was blocked and the mercury-argon lamp was positioned in the sample chamber. Once the first emission scan was taken, the user interface in the Fluorolog's software allowed the measured peaks to be matched with their accepted locations in the mercury-argon spectrum. Once properly calibrated, a final scan of the mercury-argon lamp was taken from 300 to 800 nm, which can be seen in figure 10. The locations of peaks closely resemble their accepted values which are listed in table 2. The most accurate measurements occurred near the middle of this region and all the measurements were within 1.2 nm of their accepted values which is an acceptable amount of error because the absorption and emission bands reported in this thesis are much broader in wavelength than any spectral error in the region.

Once the spectral calibration of the exit monochromator was achieved, the exit
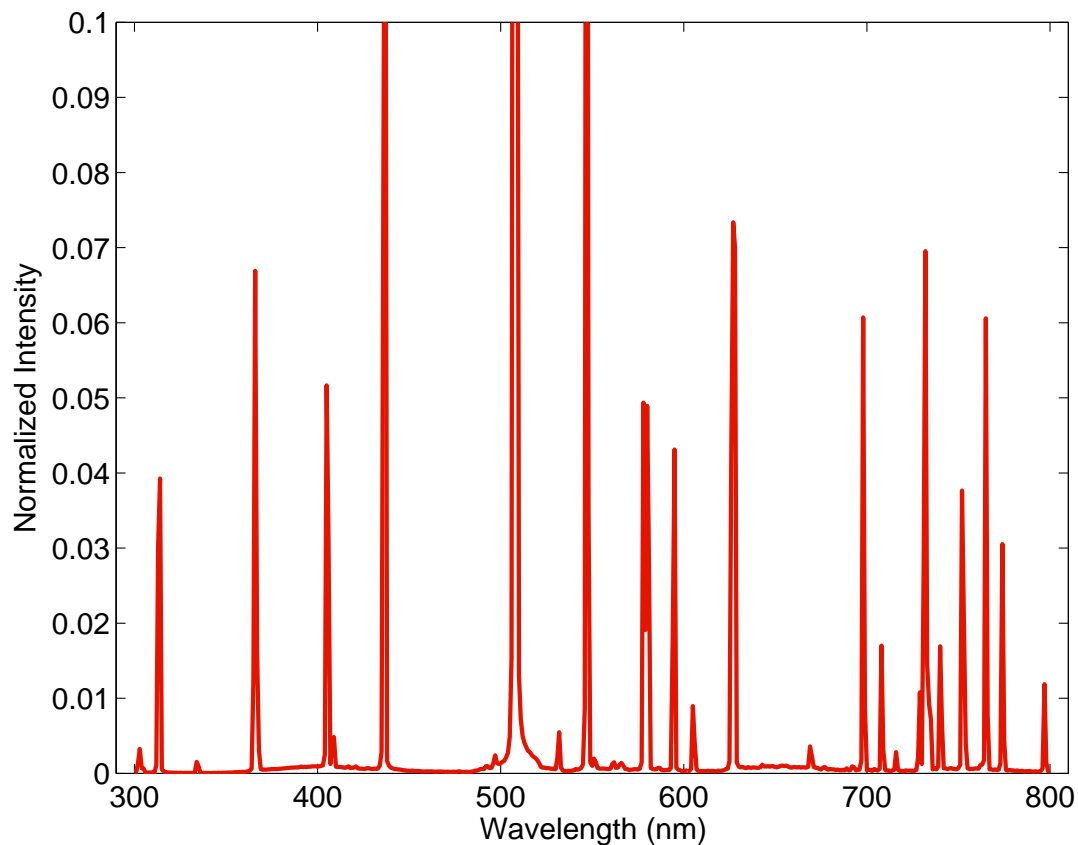
Figure 10. Spectrum of the Ocean Optics HG-1 Mercury Argon Calibration Source taken with the Fluorolog exit monochromator. The height of the tallest peak has a relative intensity of one.

measured	accepted	measured	accepted
302	302.2	604	302.1*2
313	313.2	626	313.1*2
333	334.1	668	334.1*2
365	365.0	697	696.5
404	404.6	707	706.7
436	435.8	739	738.4
507	253.7*2	751	750.4
546	546.1	764	763.5
577	577.0	773	772.4
579	579.0	796	764.8
594	298.7*2		

Table 2. Locations of the peaks in the Hg-Ar spectrum measured by the Fluorolog's exit monochromator along with the accepted values. All measurements are given in nm. Some peaks in the measured spectrum are the second order of a shorter wavelength peak which is indicated by "*2".

25

monochromator could be used for the spectral calibration of the entrance monochromator. With no sample in the chamber, the exit monochromator was set to monitor a specific wavelength while the entrance monochromator scanned through a range of wavelengths including the monitored wavelength. The entrance monochromator was then calibrated so that the single spike aligned with the monitored wavelength (an example can be seen in figure 11). The most accurate calibration (within 1 nm) was chosen for the 200 to 400 nm region because this is where the majority of excitation bands occur.

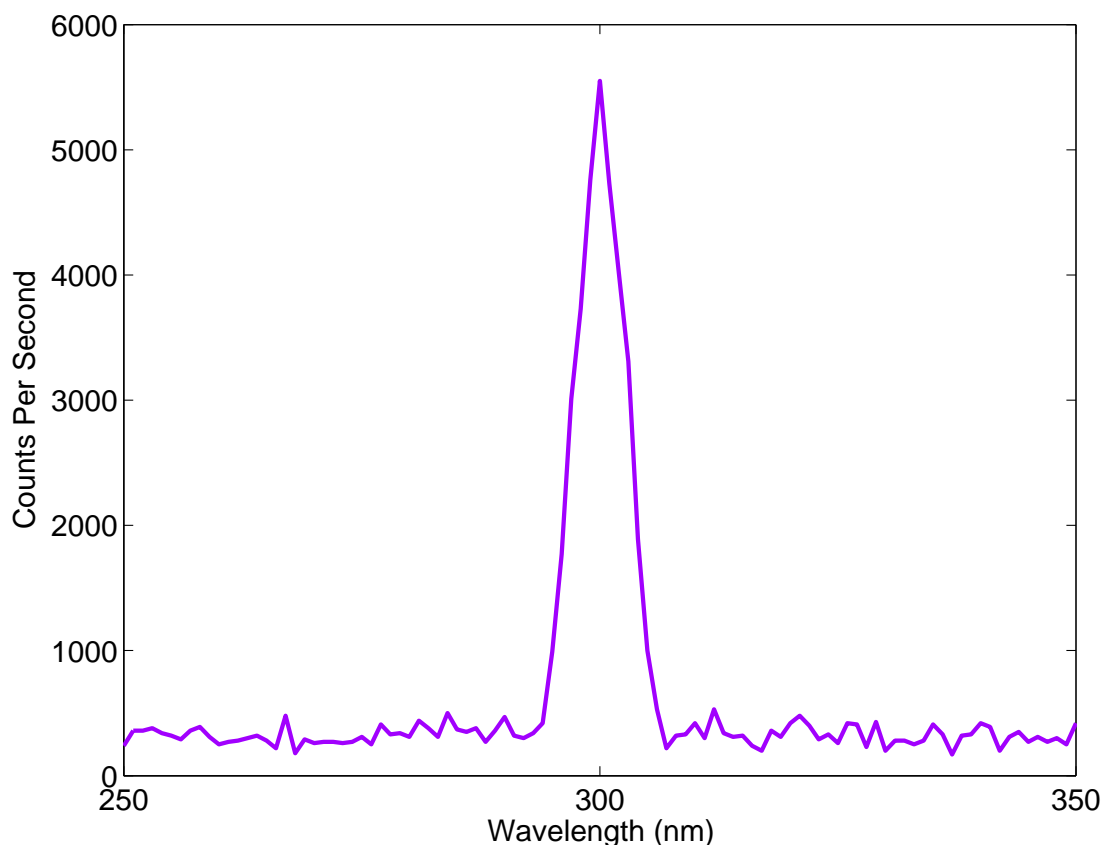
Figure 11. PLE scan monitoring 300 nm with no sample or holder in the sample chamber. The peak position at the same wavelength as the monitoring wavelength indicates proper spectral calibration of the entrance monochromator.

In addition to spectral calibration, the intensity values for the data in both the excitation and emission spectra required correction. The ideal excitation monochro-

mator would produce an equal number of photons at every wavelength in the region of interest. Actual excitation monochromators, however, produce varying output at different wavelengths due to the characteristics of the diffraction gratings and mirrors in conjunction with the wavelength dependence of the power output of the xenon lamp. The correction for constant photon flux can be determined by the following:

$$\text{Power} = \frac{E_{\text{total}}}{t} = \frac{N}{t} E_{\text{photon}} = \frac{N}{t} \frac{hc}{\lambda n}, \tag{14}$$

where N represents the number of photons and n represents index of refraction, assumed to be 1.00. If there were constant photon flux across all wavelengths then:

$$\text{Power} * \lambda = \frac{N}{t} \frac{hc}{n} = \text{constant}. \tag{15}$$

Therefore, the raw data can be corrected for constant photon flux by dividing the data by the following factor:

$$I_{\text{measured}} \div (\text{Power} * \lambda) = I_{\text{actual}}. \tag{16}$$

The power output of the Fluorolog's xenon light, through the excitation monochromator, in the wavelength region of interest, was measured using the Fluorolog's built-in photo-diode, which is displayed as the orange curve in figure 13. The correction factor (Power $* \lambda$) peaks in the 2.47-3.10 eV (400-500 nm) region, therefore, the PLE correction tends to magnify the features farthest from this region and move the peak away from this region, as seen in the corrected PLE curve in figure 12.

Intensity values in the emission spectra also had to be corrected for the wavelength dependence of the efficiency of the diffraction gratings, mirrors, and sensitivity of the photomultiplier tube. For the purpose of this study these factors were combined

27
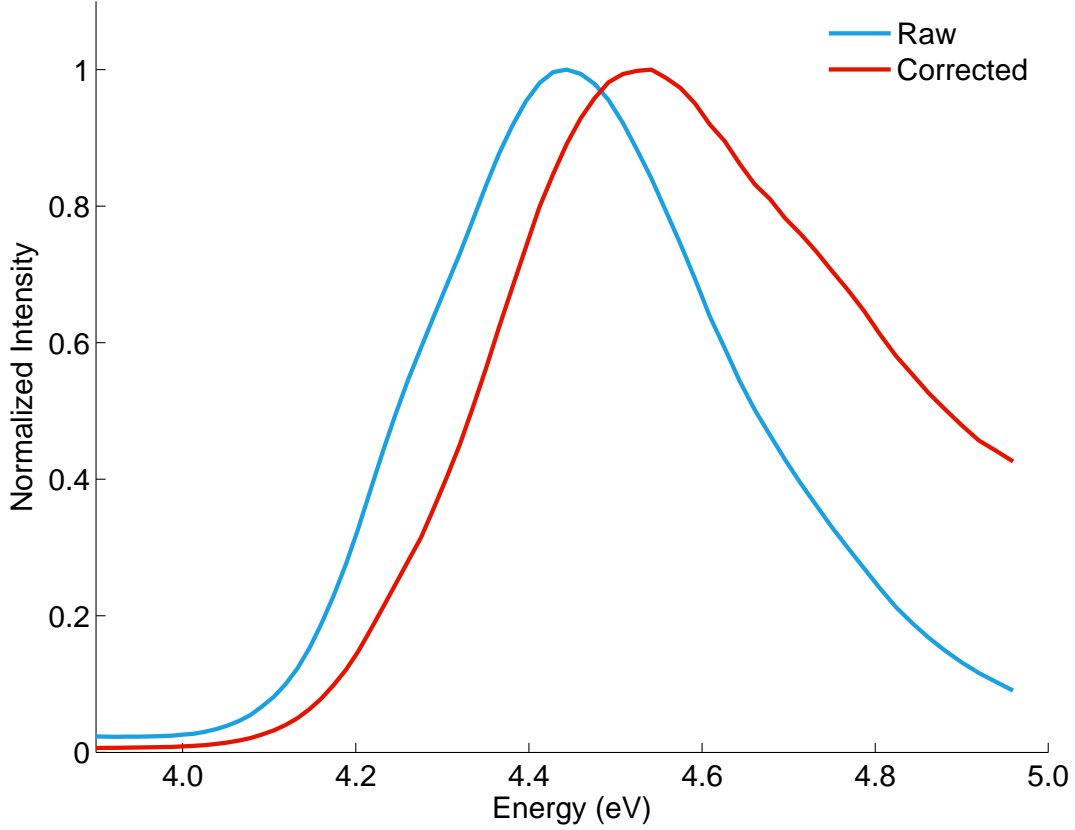
Figure 12. PLE of LiAlO$_2$:Cu obtained by monitoring the emission at 365 nm. Entrance slit resolution: 2 nm, Exit slit resolution: 5 nm.

into one factor called system response. System response modifies the actual intensity measurements according to the following equation:

$$I_{\text{actual}} \cdot I_{\text{system response}} = I_{\text{measured}}. \tag{17}$$

For calibration purposes, both an actual and measured spectrum were required to determine system response. The actual intensity curve, I_{actual}, was obtained by measuring the output of the xenon lamp using the Fluorolog's R1 detector, a photo-diode that is located in front of the sample chamber (this data is illustrated as the orange curve in figure 13). The measured intensity curve, I_{measured}, was obtained by conducting synchronous scans with the Fluorolog. During a synchronous scan, both the

28
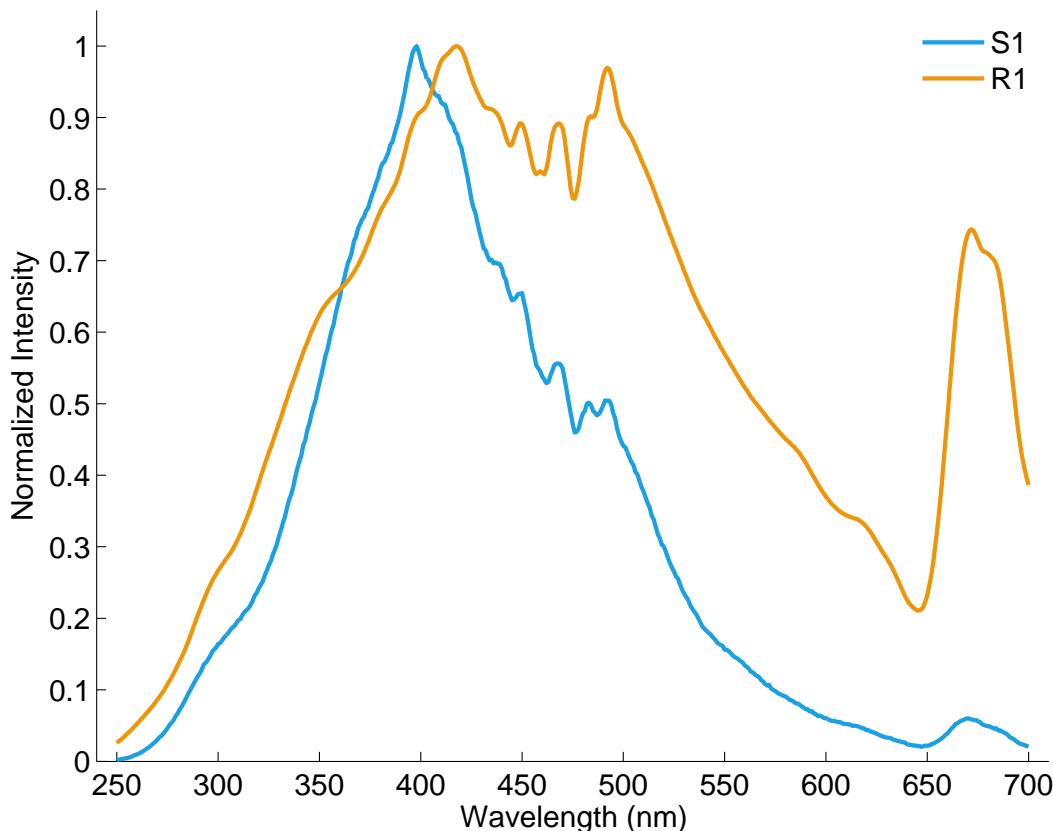
Figure 13. Spectra of the Fluorolog's xenon excitation lamp through the entrance monochromator, measured with the Fluorolog's R1 photo-diode, and through the entrance and exit monochromators, measured with the Fluorolog's photomultiplier tube (referred to as the S1 detector in the Fluorolog's software).

entrance and exit monochromators scan through the same wavelength range simultaneously. With no sample in the chamber during the synchronous scan, the photomultiplier tube only measured the light from the xenon lamp after it had passed through both the entrance and exit monochromators set to the same wavelength. The average intensity values over five synchronous scans are displayed in figure 13 as the blue curve.

The actual and measured intensity curves were used to calculate the system response curve using equation 17. The result is displayed as the magenta curve in figure 14. The smooth green curve in the same figure is a twentieth degree polynomial that was created by applying a least squares regression to the magenta curve

(twenty is a degree that provided a good fit to the data without much oscillation near the edges). This polynomial served as the final $I_{\text{system response}}$ by which all of the PL scans in this study were corrected. The system response polynomial peaks near 3.10 eV (400 nm), thus its correction causes the magnification of features far from this value and shifts peaks away from this value as can be seen in the corrected red PL curve in figure 15.
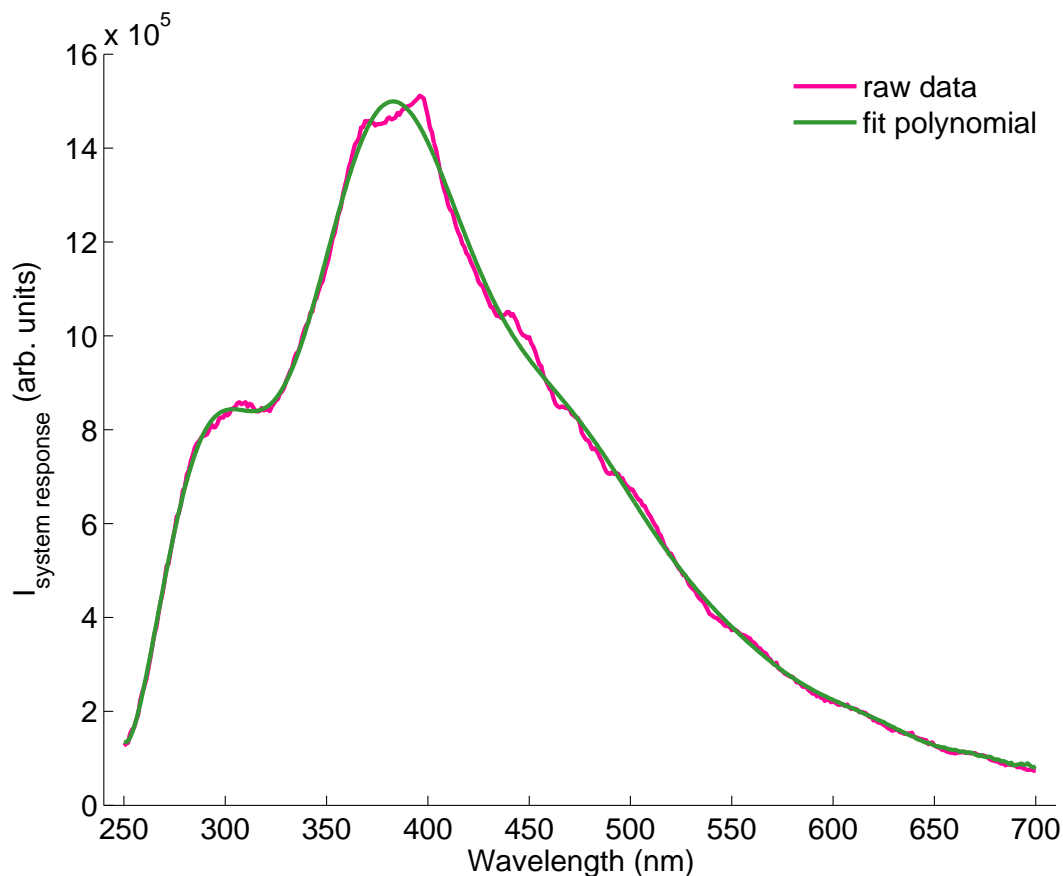
Figure 14. Exit monochromator system response. The raw curve was obtained by dividing the two curves in figure 13.

Another correction was required in order to correctly represent an intensity emission spectrum with respect to energy. Using the Fluorolog spectrophotometer, intensity data is taken as I_λ versus λ where a single data point is a representation of intensity over a specific interval of wavelengths, written as $I_\lambda d\lambda$. In order to plot I_E
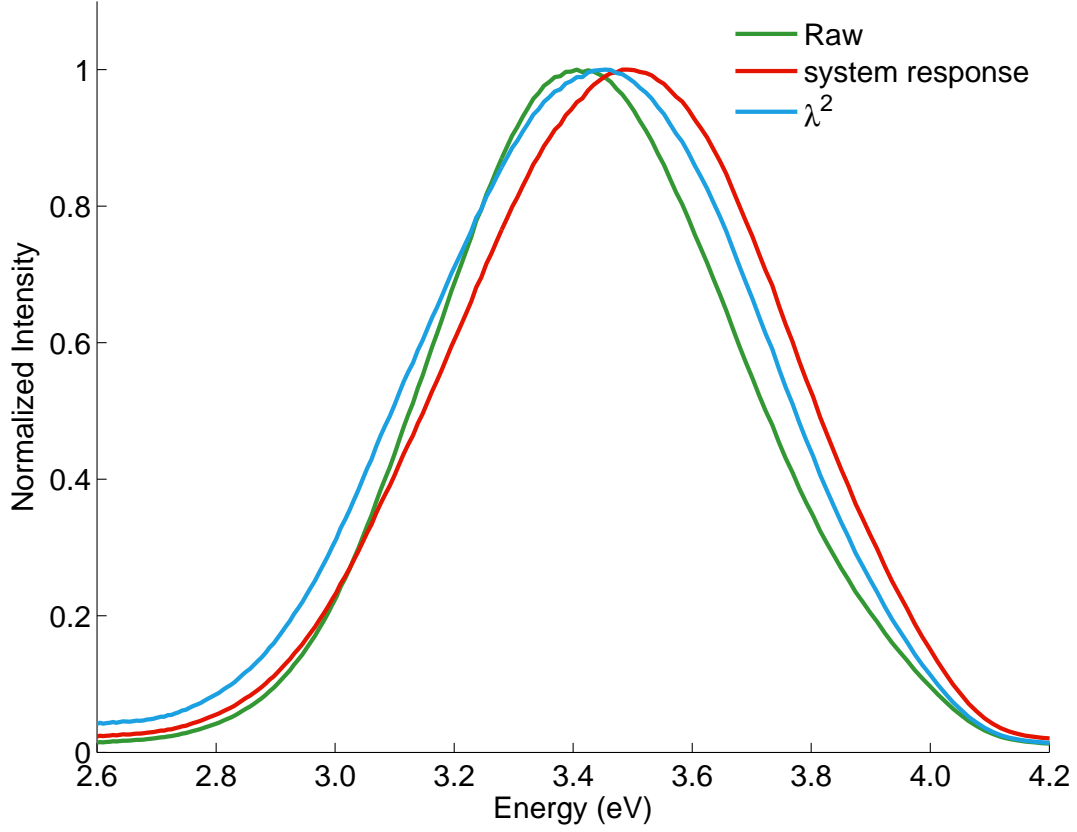
Figure 15. PL of LiAlO$_2$:Cu taken during 270 nm excitation. Entrance slit resolution: 2 nm, Exit slit resolution: 5 nm. The λ^2 correction was applied after the system response correction.

versus E, dE must be determined:

$$E = \frac{hc}{\lambda} \tag{18}$$

$$\mathrm{d}E = \frac{hc}{\lambda^2}\mathrm{d}\lambda \tag{19}$$

The following relationship between I_E and I_λ, which is obtained by substituting the previous equation, is known as the λ^2 correction [17, 26]:

$$I_E\mathrm{d}E = I_E\frac{hc}{\lambda^2}\mathrm{d}\lambda = I_\lambda\mathrm{d}\lambda \tag{20}$$

$$I_E = I_\lambda\frac{\lambda^2}{hc}. \tag{21}$$

Each emission spectrum is corrected by dividing it by the previously mentioned system response curve and multiplying it by a factor proportional to λ^2. The constants h and c are not accounted for in this factor, thus most spectra in this thesis are plotted in arbitrary units with respect to energy in electron volts. The effect of the λ^2 correction is more dramatic on wider emission bands and tends to move the peak location to lower energies (higher wavelengths) which is shown by the blue curve in figure 15.

4.3   Sample Preparation

All of the $LiAlO_2$ and $LiGaO_2$ samples used in this study were purchased from the MTI Corporation (Richmond, CA). The company supplied undoped, 0.5 mm thick c plates, with both sides machine polished. The plates were then cut into 3 mm $\times$ 5 mm pieces so that they could fit into the EPR spectrometer. Copper was diffused into some of the samples by wrapping them with copper foil, then using a tube furnace to heat them to 900 °C in nitrogen for two hours. After the two-hour period, the samples were allowed to quickly cool to room temperature.

V. Results and Discussion

5.1 Lithium Aluminate

DIFFUSING copper into $LiAlO_2$ crystals, using the technique described in section 4.3, results in a PL band that peaks at 3.45 eV (359 nm) and a corresponding PLE band that peaks at 4.54 eV (273 nm). The Stokes shift for these bands is 1.09 eV. Figure 16 shows that the PL and PLE signals from the the copper-diffused crystals are significantly stronger than those from the as-grown crystals.
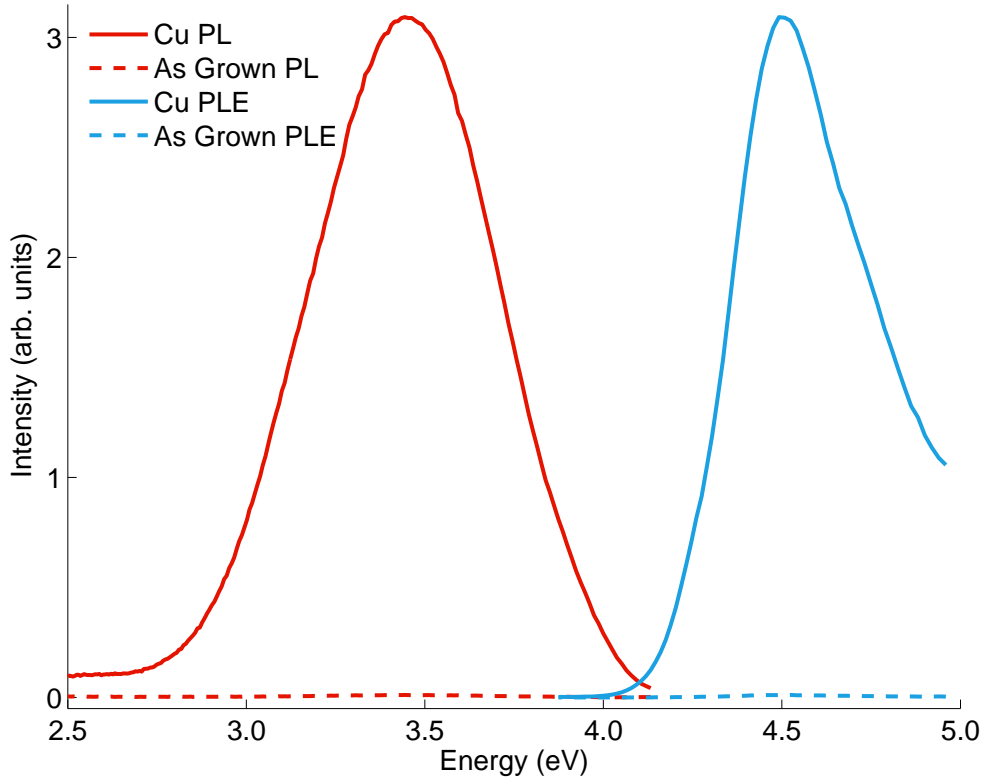
Figure 16. PL and PLE of as-grown and copper-diffused $LiAlO_2$. PL excitation wavelength: 270 nm. PLE monitored wavelength: 360 nm. Entrance slit resolution: 1 nm. Exit slit resolution: 5 nm.

The PL signal is well described by a single Gaussian function, from which, the full width at half maximum (FWHM) was determined to be 0.68 eV. The PLE signal could not be fit to one Gaussian function (although two Gaussians provide a good fit)

due to the shoulder on the high energy side of the band, so its FWHM was determined to be 0.55 eV by graphical inspection.

An analysis of the shape of the emission curve can be performed using the theory discussed in section 2.3. The zero phonon line is assigned the energy 4.11 eV (where the PL and PLE curves intersect) and the PL peak is assigned the previously mentioned value of 3.45 eV. Assuming that the only Raman mode associated with this Stokes shift is the Li-O stretching mode at 398 cm^{-1}, identified by Qiwei Hu et al. [27], an estimation of the S value can be made:

$$398\,\text{cm}^{-1} \cdot 3 \times 10^{10}\,\text{cm/s} \cdot 4.136 \times 10^{-15}\,\text{eV s} = 0.0494\,\text{eV}, \qquad (22)$$

$$S \approx \frac{\text{zero phonon line} - \text{peak}}{\text{Raman Mode}} = \frac{4.11\,\text{eV} - 3.45\,\text{eV}}{0.0494\,\text{eV}} = 13.4. \qquad (23)$$

This value agrees with the Gaussian shape of the emission curve (emission curves become Gaussian as S values increase above 10, as seen in figure 5). The calculation above only considers the bulk mode caused by the interaction of lithium and oxygen. The interaction between copper, substituting for lithium, and oxygen would be of lower energy because heavier copper ions would lead to slower oscillations.

Both the PL and PLE bands of the copper-diffused samples match similar PL measurements taken by Y. Fujimoto on copper-doped LiAlO$_2$ single crystals [3]. Also, the appearance of the PLE band after copper diffusion matches the appearance of the ultraviolet absorption band measured at AFIT by M. S. Holston after copper diffusion (as seen in figure 17) [28]. These consistencies suggest that the PL and PLE bands are the result of Cu$^+$ ions substituting for Li$^+$ ions.

PL scans were conducted with a series of excitation wavelengths from 250 nm to 290 nm to examine whether there were multiple emission bands. As seen in figure 18, there is no shift in peak position which shows that only one emission band is present
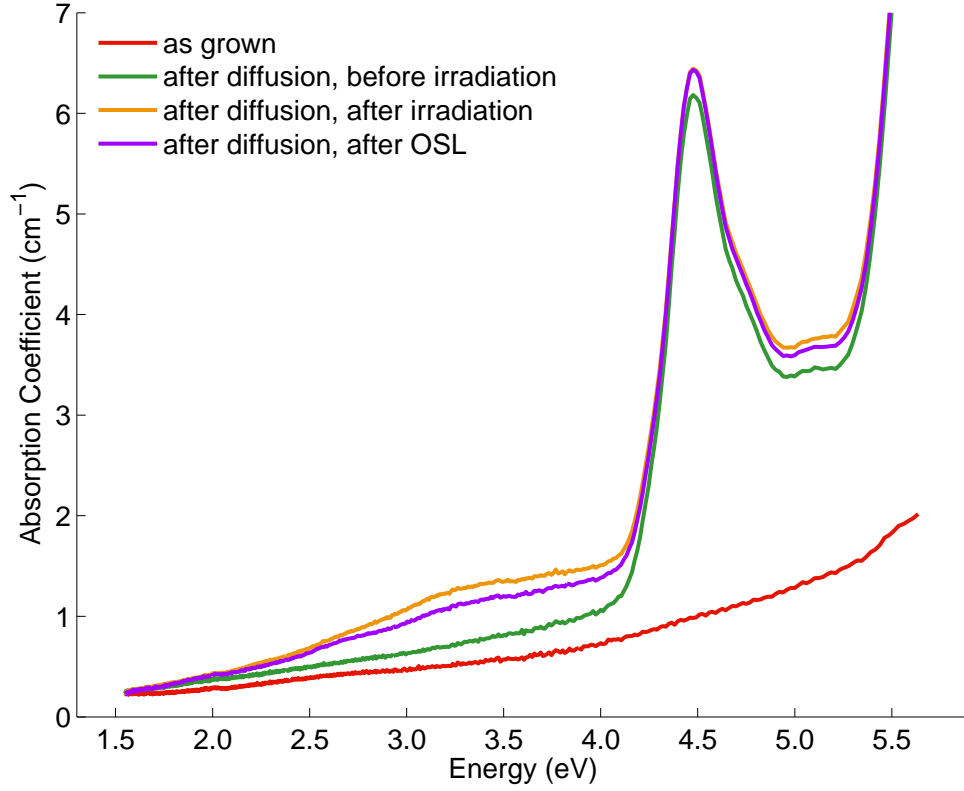
Figure 17. Absorption data for LiAlO$_2$ in as-grown and copper-diffused states, before and after x-ray irradiation and OSL bleaching. Data taken with a Cary-5000 spectrophotometer.

in the energy range from 2.5 eV to 4 eV. The strongest signals are those where the excitation wavelength was the closest to the uncorrected position of the the PLE signal, thus the 280 nm excitation produced the largest signal. The abnormal shape at the edges of the 290 nm excitation curve is the result of increased stray light when the wavelength of the excitation light was closer to the emitted wavelengths being monitored.

A similar survey of the PLE curves, where the monitored wavelength was adjusted from 340 nm to 380 nm, can be seen in figure 19. Here too, the consistency in the peak location suggests that there is only one excitation mechanism in the 3.8 eV to 5 eV range. The relative strength of the 360 nm monitored curve is similar to the location of the PL peak. The presence of one excitation mechanism and one
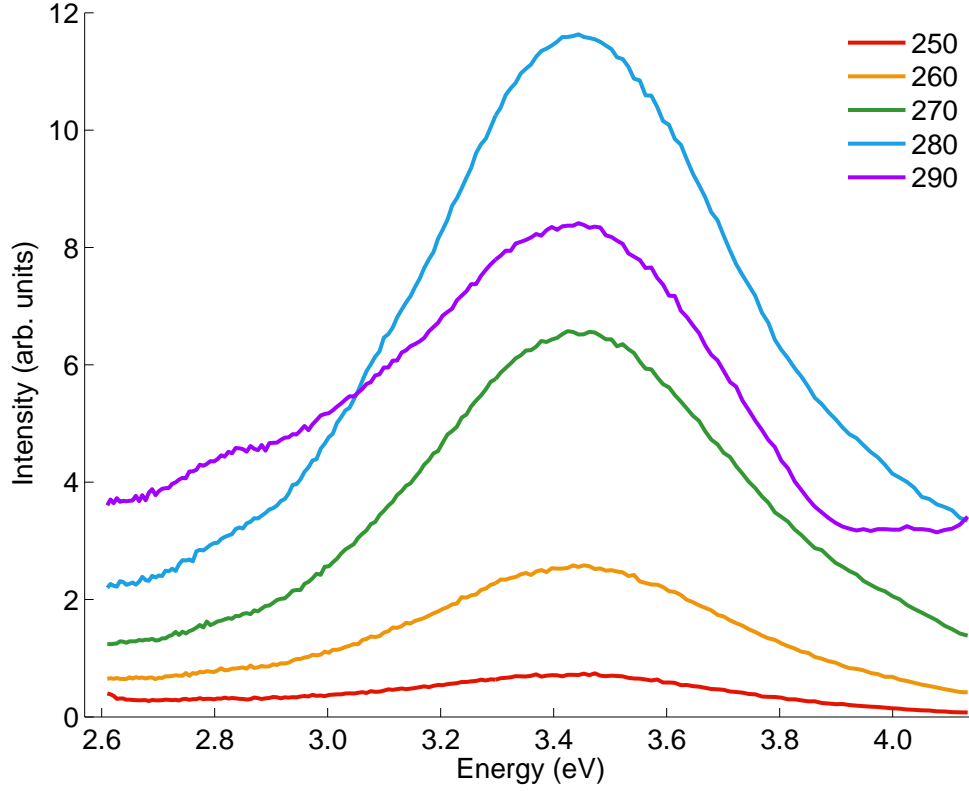
Figure 18. PL of LiAlO$_2$:Cu with various excitation wavelengths (in nm). Entrance slit resolution: 1 nm, exit slit resolution: 5 nm.

emission mechanism suggests one recombination process for the fluorescence of the copper-diffused material in this energy region.

Following exposure to x-rays at room temperature, the LiAlO$_2$ crystals exhibited OSL signals. Figure 20 shows that the strength of the OSL response in the copper-diffused samples was significantly larger than the response from the as-grown samples. Both curves are nonexponential and appear to follow the stretched exponential mentioned in section 3.3, though a rigorous analysis of the mathematical function representing the curves was not conducted as a part of this thesis.

A survey of the optimum stimulation wavelength was conducted by irradiating the copper-diffused LiAlO$_2$ with x-rays for one minute, observing the OSL signal with a certain stimulation wavelength, then annealing the sample at 500 °C for twenty minutes to empty any remaining traps. The results of this survey are presented in
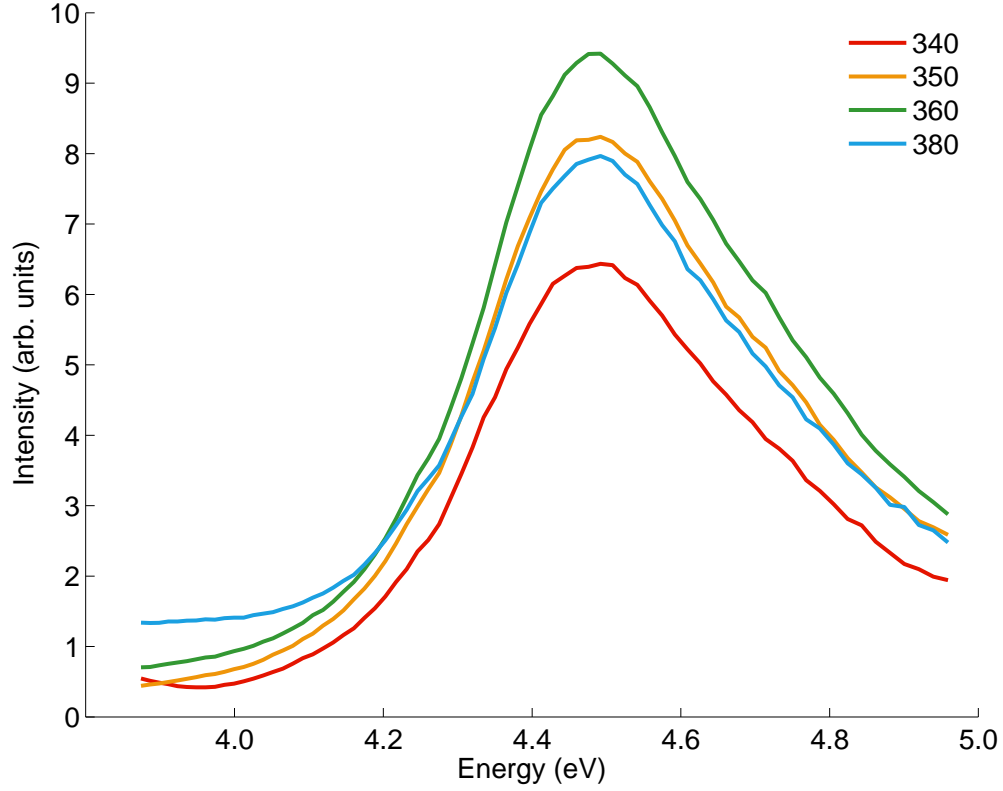
Figure 19. PLE of LiAlO$_2$:Cu monitored at various wavelengths (in nm). Entrance slit resolution: 1 nm, exit slit resolution: 5 nm.

figure 21. Judging the strength of the signal by its initial value (when the crystal is first exposed to the stimulating light), the OSL response is largest for the stimulation wavelengths closest to 400 nm. The signal strength also decreases consistently up to 525 nm. These findings match M. S. Holston's measurements of x-ray irradiated, copper-diffused LiAlO$_2$ which show a wide absorption band that gradually increases in the 400 to 500 nm range [28] (see figure 17).

The spectral dependence of the OSL signal was also measured using repeated PL scans where the excitation wavelength was set to 425 nm and the emission monochromator was set to monitor from 300-400 nm repeatedly. The results are displayed in figure 22. Each scan took 6.5 s causing a decrease in intensity from one scan to the next. Each signal has approximately the same peak position, but the first few appear to be slightly shifted towards high energy. This is because each scan begins

Figure 20. First 60 s of OSL response for as-grown and copper-diffused LiAlO$_2$. Stimulation wavelength: 450 nm. Entrace slit resolution: 10 nm. Exit slit resolution: 10 nm.
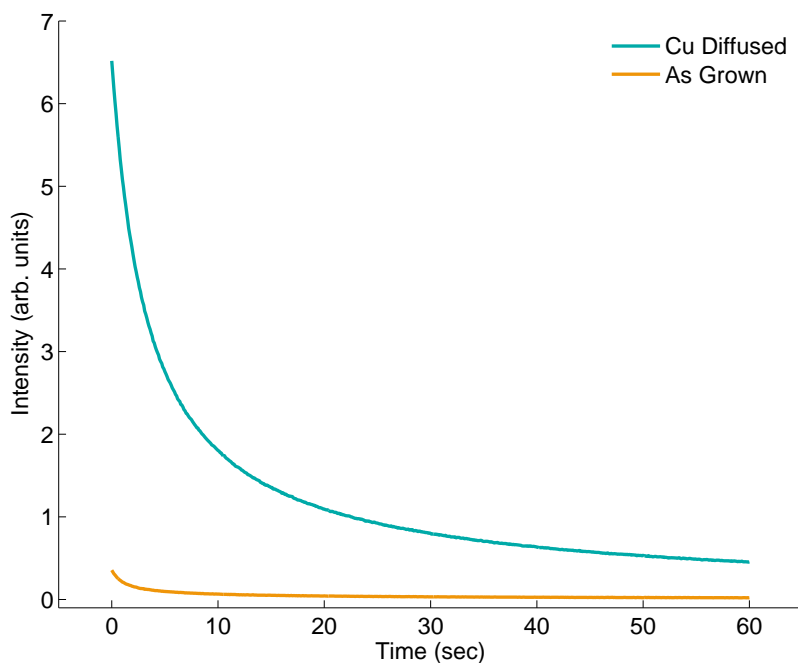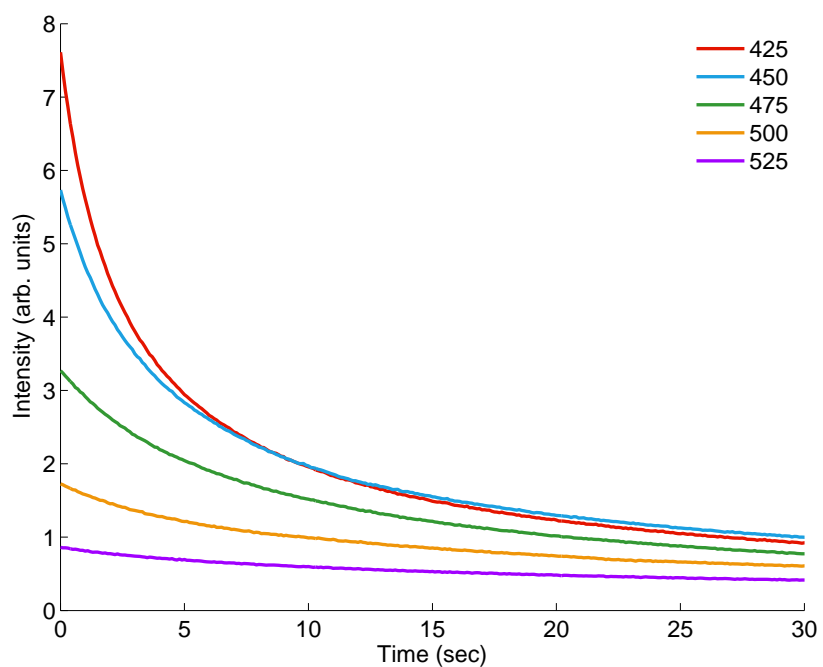

Figure 21. First 30 s of OSL response for LiAlO$_2$:Cu with various stimulation wavelengths (in nm). Entrance slit resolution: 10 nm, exit slit resolution: 10 nm.

at the high energy side of the plot then takes about 3 s before it is measuring the light near the peak. During this time, the total OSL intensity has decreased, causing the high energy side to be slightly higher than the opposite side. This effect becomes less significant as time progresses, thus the smaller curves more accurately depict the symmetrical shape of the OSL signal. The spectral dependence of the OSL signal has a peak position of 3.47 eV (357 nm) and a FWHM of 0.63 eV. These values establish a similarity between the OSL and PL signals and allow the conclusion that they both occur due to recombination at Cu^+ sites.
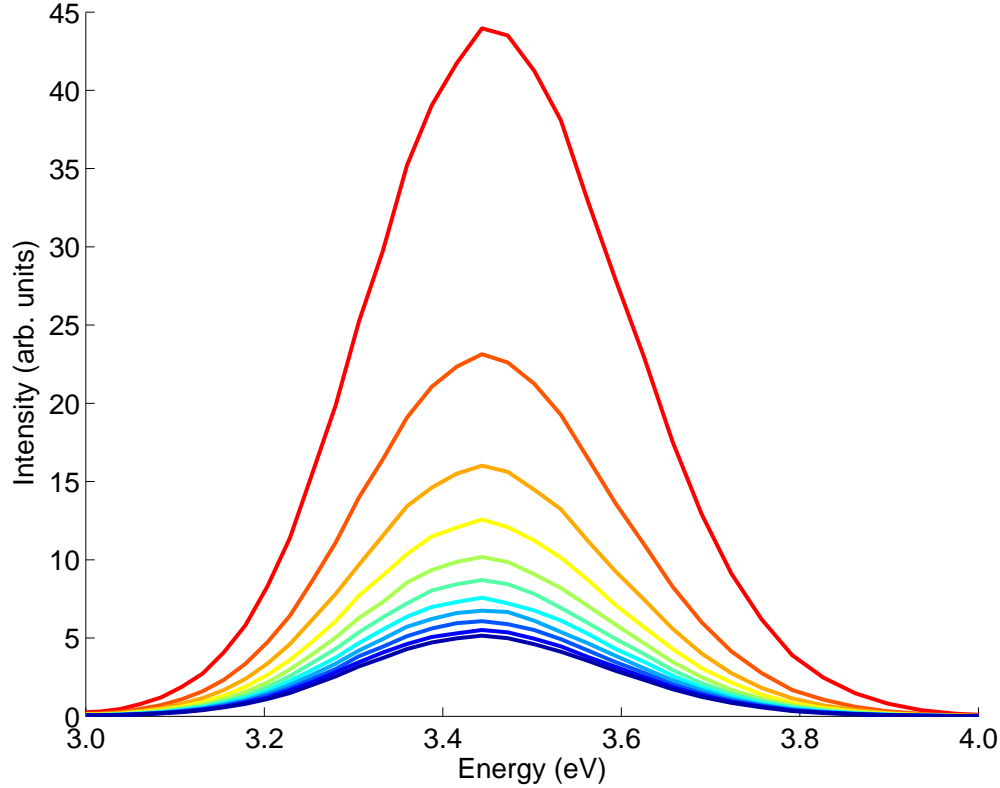
Figure 22. **Spectral dependence of the LiAlO$_2$:Cu OSL signal. Several scans each lasting 6.5 sec were taken consecutively. Stimulation wavelength: 425 nm, entrance slit resolution: 10 nm, exit slit resolution: 10 nm.**

The specific defects that caused the PL, OSL, and absorption behavior were identified using electron paramagnetic resonance (EPR) spectroscopy. As-grown crystals show no significant EPR signal in the 300 to 380 mT region (with microwave frequency

Figure 23. EPR signal showing Cu^{2+} ions in copper-diffused $LiAlO_2$. The data were taken by M.S. Holston using a Bruker EMX spectrometer at 28 K with the magnetic field in [001] direction. Plot (a) shows the sample after x-ray irradiation, before OSL. Plot (b) shows the sample after x-ray irradiation followed by optical stimulation for three minutes.

9.401 GHz), but several lines appear after copper-diffusion and x-ray irradiation (see figure 23). The eleven-line spectrum from 326 to 336 mT was previously identified as a trapped hole on a oxygen site adjacent to a lithium vacancy (intrinsic defect) which interacts with its two neighboring aluminum ions [28]. This signal has been measured in undoped $LiAlO_2$ crystals after exposure to x-rays. The remaining lines in figure 23 are the result of Cu^{2+} ions (Cu^+ ions do not cause an EPR signal because they contain no unpaired electron spins). The two stable copper isotopes, ^{63}Cu and

^{65}Cu, both have $I = 3/2$ nuclear spins which result in four line hyperfine patterns. The magnetic moments of the two isotopes are slightly different which causes the spacing of the four hyperfine lines to be different for the two isotopes. On the edges of the plot, where the ^{63}Cu and ^{65}Cu lines are clearly resolved, the ^{63}Cu line is twice as intense as the ^{65}Cu line because ^{63}Cu has roughly twice the natural abundance of ^{65}Cu. Isolated Cu^{2+} ions produce a different signal (red stick diagram in figure 23) from Cu^{2+} ions located next to a lithium vacancy (blue stick diagram). A similar effect is observed in $Li_2B_4O_7$ [29]. The decrease in the isolated Cu^{2+} EPR signal, after optical stimulation with 425 nm light for three minutes, indicates that one trap involved with the OSL behavior is a Cu^+ ion that traps a hole to become Cu^{2+}.
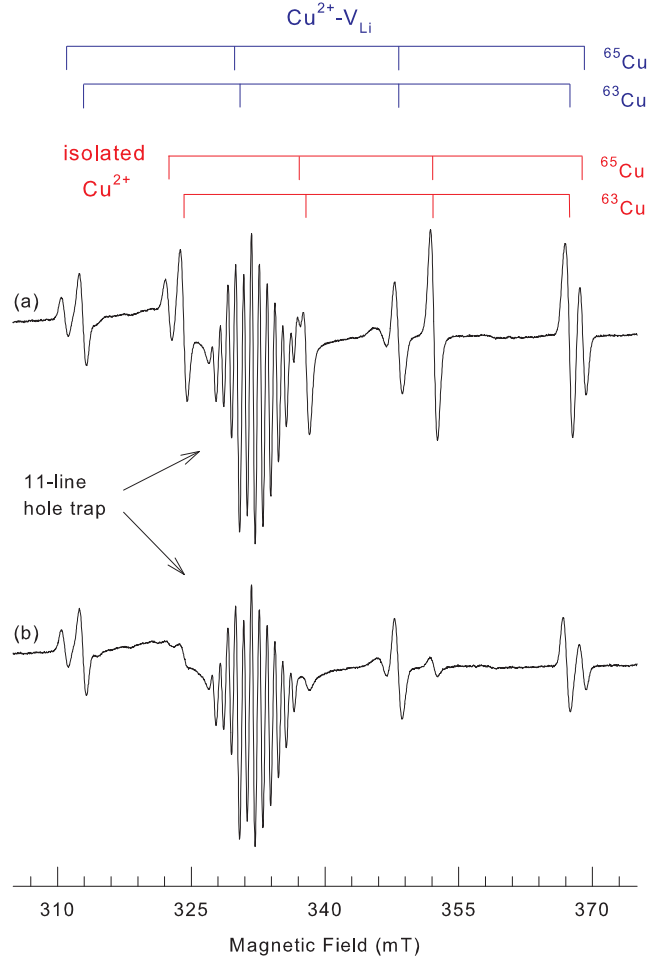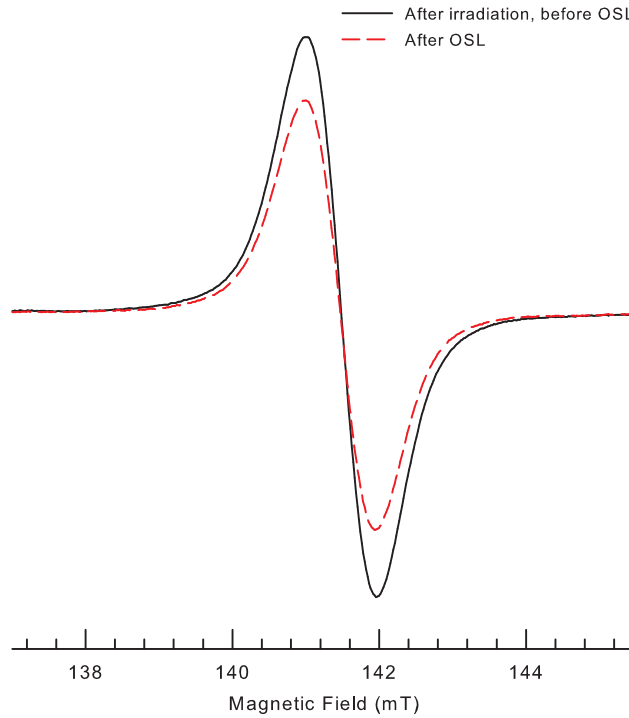

Figure 24. EPR signal showing Fe$^+$ ions in copper-diffused LiAlO$_2$. The data were taken by M.S. Holston using a Bruker EMX spectrometer at 15 K with the magnetic field in the [001] direction.

The electron trap involved in the OSL process was also identified using EPR spectroscopy. Figure 24 shows a single line centered at 141.5 mT (microwave frequency

9.401 GHz) that is present in the as-grown and copper-diffused crystals after x-ray irradiation. M.S. Holston's study of the angular dependence of this EPR signal showed a large g shift between principal axes of the crystal that is characteristic of transition metal ions including Fe^+, Co^{2+}, and Ni^{3+} [30]. Of these three, Fe^+ is the most likely candidate because this signal does not match the distinct Co^{2+} signal due to its $I = 7/2$ nuclear spin and Ni^{3+} is rarely found in oxide crystals. Furthermore, Fe impurities have been found in nominally undoped, irradiated $LiAlO_2$ crystals in previous studies [31]. Additional lines result from iron's true electron spin of $S = 3/2$, but they are so spread out that they cannot be measured with the EPR spectrometer's magnetic field range. Before x-ray irradiation, the signal in figure 24 is not present. Also, the signal's intensity decreases after optical stimulation with 425 nm light. This suggests that the Fe^{2+} ions (which are not visible with EPR spectroscopy) trap electrons during x-ray irradiation and become Fe^+ ions which produce the 141.5 mT line, then release the electrons during stimulation causing this line's intensity to decrease.

The OSL behavior of copper-diffused $LiAlO_2$ crystals can be summarized with the following steps (pictured in figure 25): x-ray irradiation causes Fe^{2+} defects to trap an electron and become Fe^+ while Cu^+ defects trap a hole and become Cu^{2+}. 425 nm light is absorbed by the Fe^+ which becomes Fe^{2+} after releasing an electron. The free
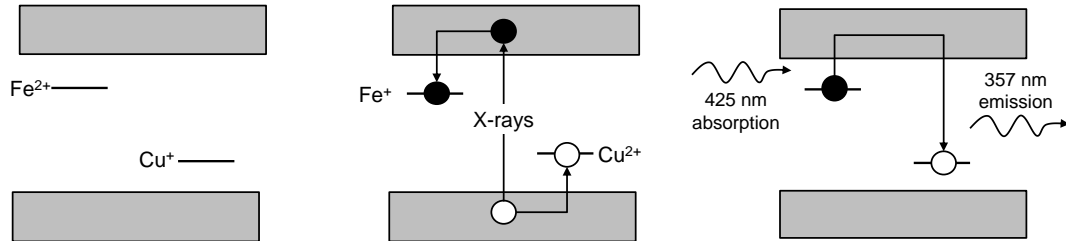
Figure 25. **Summary of the OSL process in copper-diffused $LiAlO_2$.** **Black circles indicate electrons, white circles indicate holes, gray boxes indicate energy bands.**

electron recombines with its hole causing Cu^{2+} to become $(Cu^+)^*$. This excited state relaxes by emitting 357 nm light.

5.2 Lithium Gallate

The diffusion of copper into $LiGaO_2$ crystals produces an emission band centered at 2.33 eV (532 nm) and an excitation band centered at 3.50 eV (354 nm). The PL and PLE signals for these bands are considerably larger in the copper-diffused samples than the as-grown samples, as seen in figure 26. The Stokes shift of 1.17 eV is similar to the Stokes shift that is observed in copper-diffused $LiAlO_2$. There is also similar spacing between the band gap energy and the excitation band energy in both materials. The PL curve is a close match to a Gaussian function with a
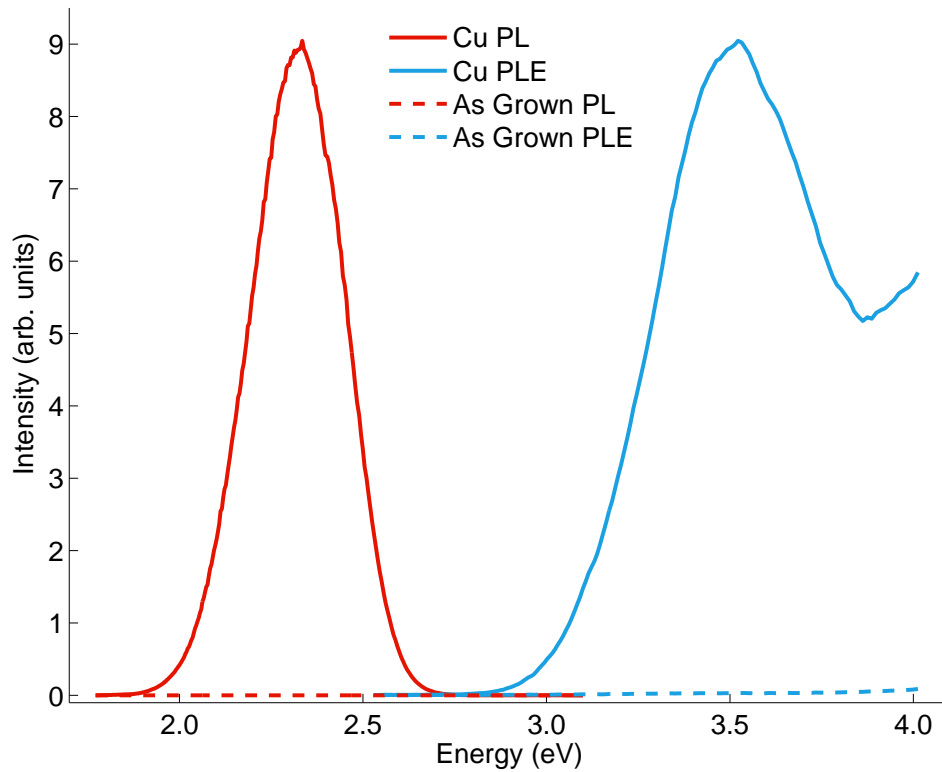
Figure 26. PL and PLE of copper-diffused and as-grown $LiGaO_2$. PL Excitation wavelength: 360 nm, PLE monitored wavelength: 525 nm. Entrance slit: 1 nm, exit slit: 5 nm.

FWHM of 0.31 eV. The FWHM of the PLE curve was determined to be 0.65 eV by graphical inspection because it is not a close match to a single Gaussian. Both FWHM values differ from those found in the PL and PLE signals for $LiAlO_2$. Furthermore, the excitation band is wider than the emission band in $LiGaO_2$, while the opposite occurs in $LiAlO_2$. Thus, the PL and PLE signals for $LiGaO_2$ are not necessarily the result of the same mechanism that produces PL and PLE in $LiAlO_2$.

This study was unable to measure an OSL signal from either the copper-diffused or as-grown $LiGaO_2$ crystals. There were also no obvious changes in the optical absorption or the EPR spectra of the material after x-ray irradiation or optical stimulation, so the defect causing the fluorescence could not be determined using the same methodology from section 5.1.

5.3 Future Work

Copper-diffused $LiAlO_2$ crystals seem to be promising OSL dosimeters based on the findings of this thesis. Future studies may attempt to discover whether a more intense OSL signal can be achieved by diffusing copper into the crystals at different temperatures, doping the crystals with copper during growth, or pre-irradiation before diffusion. In order to determine the feasibility of $LiAlO_2$ as a neutron detector, a better understanding of the material's PL and OSL behavior after neutron irradiation should be investigated.

Currently, it is not clear whether the changes in the $LiGaO_2$ crystals' PL signals are the result of copper defects, x-ray irradiation, the annealing process or some combination of the three. A systematic approach using several crystals should help to isolate the causes and provide insight into the defects formed in $LiGaO_2$. The green thermoluminescence caused by excitation with 325 nm light in both the as-grown and copper diffused samples should also be investigated.

Finally PL and OSL studies of both materials should be conducted after diffusion with silver. Another oxide crystal containing lithium, $Li_2B_4O_7$, produced interesting PL effects when doped with copper and silver [32]; perhaps $LiAlO_2$ and $LiGaO_2$ will as well.

Appendix A. Fluorolog Xenon Lamp Output Power

The following power (PWR) data for the Fluorolog's xenon lamp was taken by D.A. Buchanan with an external power meter (with both ultraviolet and visible detector heads) placed in the Fluorolog's sample chamber [33]. The switch between heads occurs at 399 nm where there are two measurements taken. This data is similar, but not equivalent to that taken using the built-in R1 photo-diode.

λ (nm)	PWR (mW)	λ (nm)	PWR (mW)	λ (nm)	PWR (mW)
250	0.007	399	0.288	540	0.134
255	0.015	399	0.287	545	0.127
260	0.024	400	0.285	550	0.120
265	0.036	405	0.288	555	0.114
270	0.048	410	0.298	560	0.108
275	0.060	415	0.295	566	0.102
281	0.078	420	0.297	571	0.098
285	0.087	425	0.280	575	0.093
290	0.101	430	0.269	580	0.090
295	0.113	435	0.259	585	0.086
300	0.122	440	0.256	590	0.081
305	0.128	445	0.240	596	0.074
311	0.138	450	0.258	600	0.071
315	0.146	455	0.227	605	0.067
320	0.161	460	0.219	610	0.063
325	0.175	465	0.222	615	0.060
330	0.188	470	0.234	620	0.060
335	0.202	475	0.207	625	0.055
341	0.215	480	0.213	630	0.050
346	0.232	485	0.223	635	0.045
350	0.243	490	0.230	640	0.040
355	0.253	495	0.228	645	0.034
360	0.263	500	0.208	651	0.038
365	0.270	506	0.201	652	0.040
371	0.277	511	0.191	655	0.051
375	0.279	515	0.185	657	0.060
380	0.281	520	0.172	660	0.077
385	0.277	525	0.162	662	0.089
390	0.276	530	0.152	665	0.106
395	0.285	535	0.142	670	0.121

λ (nm)	PWR (mW)	λ (nm)	PWR (mW)	λ (nm)	PWR (mW)
672	0.123	790	0.016	871	0.015
675	0.122	795	0.013	874	0.018
680	0.113	800	0.013	876	0.023
685	0.110	805	0.011	877	0.029
690	0.095	811	0.011	878.5	0.046
692	0.085	815	0.012	880	0.073
694	0.076	817	0.015	882	0.102
696	0.071	818	0.019	883	0.099
698	0.067	819	0.026	885	0.065
700	0.063	820	0.039	888	0.034
705	0.055	821	0.059	890	0.031
710	0.058	822	0.076	891	0.034
715	0.052	823	0.086	893	0.054
720	0.042	825	0.075	894	0.066
725	0.039	826	0.065	896	0.067
730	0.042	827	0.059	897	0.054
735	0.037	828	0.054	899	0.033
740	0.034	829	0.043	901	0.038
745	0.029	830	0.031	902	0.052
750	0.028	831	0.025	904	0.073
755	0.025	833	0.034	905	0.069
760	0.026	836	0.029	907	0.036
765	0.037	841	0.018	908	0.027
767	0.024	845	0.007	910	0.024
770	0.018	850	0.006	913	0.053
772	0.016	855	0.007	915	0.093
776	0.015	860	0.008	918	0.080
780	0.013	865	0.010	920	0.044
785	0.013	868	0.012		

Appendix B. Fluorolog Operation Instructions

Starting the Fluorolog (for Fluorolog shutdown follow these steps in the opposite order):

1. Flip the switch to the black surge protector to start the cooler.

2. Flip the green switch on the white Eurosep Instruments box to turn the xenon lamp on.

3. Flip the switch on the back of the computer tower labeled SPECTRACO to start the photomultiplier tube.

Running a scan:

1. Start the computer labeled OPTIPLEX 780.

2. Click the FluorEssence V3.5 icon.

3. Press the $\boxed{\text{M}}$ button (experiment menu) and wait for the devices to initialize.

4. Pick one of the following:

   - Spectra: This allows you to pick from the following:

     – Emission: Pick a fixed wavelength for the entrance monochromator and range for the exit monochromator to scan through (PL scan).

     – Excitation: Pick a fixed wavelength for the exit monochromator and a range for the entrance monochromator to scan through (PLE scan).

     – Synchronous: Pick a wavelength range that both monochromators will scan through simultaneously.

   - Kinetics: Pick a fixed wavelength for both the entrance and exit monochromators and a time scale over which to take the measurements (used for OSL and lining up sample).

- 3D: This one is a series of consecutive PL scans over a range of excitation wavelengths that you pick.

- Single Point: As the name suggests, one excitation wavelength and one monitored wavelength.

5. Depending on type of scan you picked, choose the wavelengths that you want to use by filling in the different "park," "start," and "end" boxes.

6. Specify your slit resolution by filling in the boxes labeled "slit nm." Type values between 0 and 14.7. Larger values will give you less noisy, larger signals, but it will be harder to distinguish sharp features.

7. Specify increment. This will be the spacing of the x-values in your data set.

8. Click the detectors tab on the left and check the boxes of the detectors you want to use. The R1 detector is a photodiode that measures the output of the xenon lamp. The S1 detector is photomultiplier tube (you can change the voltage on the tube by double clicking the number under "HV(V)."

9. Type your integration time into the "integration time" box.

10. Click "Run."

Exit Monochromator Spectral Calibration (entrance monochromator calibration uses the same steps, but you run an excitation scan in step 1, click the "excitation" tab in step 7, and click "Calibrate Excitation 1" in step 9).

1. For exit monochromator calibration, put your calibration lamp in the sample chamber and block the xenon light from entering the chamber.

2. Run an emission (PL) scan.

3. Double click on the graph then use the data cursor (cross-hair icon) to find the apparent location of a certain peak.

4. Click the run previous experiment button located next to the $\boxed{M}$ button.

5. Click the "RTC" button in the bottom right corner next to the "Run" button.

6. Click the "Monos" button on the left side of the window.

7. Click the "emission" tab.

8. Type the apparent location of your peak into the box labeled "position control."

9. Click "Calibrate Emission 1."

10. Type the actual location of the peak into the dialog box that appears.

11. Click "OK" then click the "Cancel" button in the lower right corner.

Additional Thoughts

- Be sure to check your background signal by removing the sample, but keeping the holder in place to make sure what you are seeing is a product of the sample. The background signal can be minimized by reducing the amount of the xenon light that hits the sample holder or other objects in the sample chamber.

- Sometimes you can block the excitation light from interfering with your PL signal by putting a long-pass glass filter in front of the exit monochromator. This way you could excite at 300 nm and scan from 400-700 nm without having to worry about the second order 300 nm light.

Appendix C. PL Correction Instructions

If you are looking to correct Fluorolog PL scans in the range between 250 and 700 nm, feel free to divide your raw data by this polynomial:

$$
\begin{aligned}
p(\lambda) = (8.030*10^{-41})\lambda^{20} &\quad -(6.4971*10^{-37})\lambda^{19} &\quad +(2.3879*10^{-33})\lambda^{18} \\
-(5.2327*10^{-30})\lambda^{17} &\quad +(7.5006*10^{-27})\lambda^{16} &\quad -(7.1562*10^{-24})\lambda^{15} \\
+(4.2162*10^{-21})\lambda^{14} &\quad -(8.8434*10^{-19})\lambda^{13} &\quad -(8.578*10^{-16})\lambda^{12} \\
+(9.1116*10^{-13})\lambda^{11} &\quad -(3.3867*10^{-10})\lambda^{10} &\quad -(5.2297*10^{-8})\lambda^{9} \\
+(1.3488*10^{-4})\lambda^{8} &\quad -(0.0847)\lambda^{7} &\quad +(32.9481)\lambda^{6} \\
-(8.948*10^{3})\lambda^{5} &\quad +(1.7423*10^{6})\lambda^{4} &\quad -(2.4002*10^{8})\lambda^{3} \\
+(2.2356*10^{10})\lambda^{2} &\quad -(1.2644*10^{12})\lambda &\quad +3.2873*10^{14}
\end{aligned}
$$

It may be easiest to get the arrays for this polynomial by copying the following into MATLAB:

coef = [8.02965042959172e-41; -6.49706354946240e-37; 2.38787156327788e-33;...

   -5.23274321864668e-30; 7.50063819425609e-27; -7.15623735344087e-24;...

   4.21619367037797e-21; -8.84342255157430e-19; -8.57835958447410e-16;...

   9.11161045631503e-13; -3.38670414893597e-10; -5.22973844119809e-08;...

   0.000134883355732576; -0.0847343018104573; 32.9481454491858;...

   -8948.52712325680; 1742292.73791266; -240153828.573596;...

   22356251854.7030; -1264405102255.25; 32872920387734.2];

wavelength = 250:700; wavelength = wavelength';

correctionPoly = polyval(coef,wavelength);

If you would like to create your own polynomial, follow these steps:

1. Turn on your Fluorolog, start the Fluorolog software, and remove all items from

the sample chamber.

2. In the Fluorolog software set up a synchronous scan (press the $\boxed{\text{M}}$ button, then $\boxed{\text{Spectra}}$, then "synchronous"). Select the S1 and R1 detectors and set your desired wavelength range, increment, and slit sizes.

3. Run the scan. The R1 curve will be your I_{actual} and the S1 curve will be your I_{measured} in equation 17.

4. Use the computer to divide I_{measured} by I_{actual} to obtain $I_{\text{system response}}$.

5. Use the computer again to get a smooth system response polynomial. In matlab, you can use the following built in functions:

poly = polyfit(λ, $I_{\text{system response}}$, degree of polynomial),

correction factor = polyval(poly, λ).

Bibliography

1. S. McKeever, *Optically stimulated luminescence dosimetry*, Nuclear Instruments and Methods in Physics Research B **184**, 29 (2001).

2. S. McKeever, *Optically Stimulated Luminescence: A brief overview*, Radiation Measurements **46**, 1336 (2011).

3. Y. Fujimoto, K. Kamada, T. Yanagida, N. Kawaguchi, S. Kurosawa, D. Totsuka, K. Fukuda, K. Watanabe, A. Yamazaki, Y. Yokota, and A. Yoshikawa, *Lithium Aluminate Crystals as Scintillator for Thermal Neutron Detection*, IEEE Transactions on Nuclear Science **59**, 2252 (2012).

4. M. Nishikawa, T. Kinjyo, T. Ishizaka, S. Beloglazov, T. Takeishi, M. Enoeda, and T. Tanifuji, *Release behavior of bred tritium for $LiAlO_2$*, Journal of Nuclear Materials **335**, 70 (2004).

5. A. Twardak, P. Bilski, B. Marczewska, J. Lee, J. Kim, W. Gieszczyk, A. Mrozik, M. Sadel, and D. Wrobel, *Properties of lithium aluminate for application as an OSL dosimeter*, Radiation Physics and Chemistry **104**, 76 (2014).

6. L. V. Azaroff, *Introduction to Solids*, McGraw-Hill Book Company, Inc., New York, 1960.

7. M. Marezio, *The Crystal Structure and Anomalous Dispersion of γ-$LiAlO_2$*, Acta Crystallographica **19**, 396 (1965).

8. X. Ke, X. Jun, D. Peizhen, Z. Yongzong, Z. Guoqing, Q. Rongsheng, and F. Zujie, *γ-$LiAlO_2$ single crystal: a novel substrate for GaN epitaxy*, Journal of Crystal Growth **193**, 127 (1998).

9. M. Chou, H. Huang, and Y. F. Chang, *Defects and acoustic properties of LiAlO₂*, Applied Physics Letters **88**, 161906 (2006).

10. J. Lee, A. Pradhan, J. Kim, I. Chang, B. Kim, and K. Chung, *Characteristics of LiAlO₂ - Radioluminescence and optically stimulated luminescence*, Radiation Measurements **56**, 217 (2013).

11. J. Mittani, M. Prokic, and E. Yukihara, *Optically stimulated luminescence and thermoluminescence of terbium-activated silicates and aluminates*, Radiation Measurements **43**, 323 (2008).

12. B. Dhabekar, E. Raja, S. Menon, T. Rao, R. Kher, and B. Bhatt, *Identification of defect centres using TSL, PL, OSL and ESR in LiAlO₂ based phosphors*, Journal of Physics D **41**, 115414 (2008).

13. M. Marezio, *The Crystal Structure of LiGaO₂*, Acta Crystallographica **18**, 481 (1964).

14. P. Kung, A. Saxler, X. Zhang, D. Walker, R. Lavado, and M. Razeghi, *Metalorganic chemical vapor deposition of monocrystalline GaN thin films on β-LiGaO₂ substrates*, Applied Physics Letters **69**, 2116 (1996).

15. M. Johnson, W. Hughes, W. Rowland, J. Cook, J. Schetzina, M. Leonard, H. Kong, J. Edmond, and J. Zavada, *Growth of GaN, InGaN, and AlGaN films and quantum well structures by molecular beam epitaxy*, Journal of Crystal Growth **175**, 72 (1997).

16. T. Huang, S. Zhou, H. Teng, H. Lin, J. Wang, P. Han, and R. Zhang, *Growth and characterization of ZnO films on (001), (100) and (010) LiGaO₂ substrates*, Journal of Crystal Growth **310**, 3144 (2008).

17. J. R. Lakowicz, *Principles of Fluorescence Spectroscopy*, Kluwer Academic, New York, 2nd edition, 1999.

18. L. Wang, *Photoluminescence Study of As-grown and Thermally Annealed Bulk ZnO Crystals*, PhD dissertation, West Virginia University, Morgantown (2004).

19. E. Condon, *A Theory of Intensity Distribution In Band Systems*, Physical Review **28**, 1182 (1926).

20. B. Henderson and G. F. Imbusch, *Optical Spectroscopy of Inorganic Solids*, Oxford University Press, Oxford, 1989.

21. E. G. Yukihara and S. W. McKeever, *Optically Stimulated Luminescence: Fundamentals and Applications*, John Wiley & Sons, West Sussex, 2011.

22. D. Huntley, D. Godfreysmith, and M. Thewalt, *Optical Dating of Sediments*, Nature **313**, 105 (1985).

23. H. Grimmeiss and L. Ledebo, *Photo-ionization of deep impurity levels in semiconductors with non-parabolic bands*, Journal of Physics C: Solid State Physics **8**, 2615 (1975).

24. R. Chen and P. Leung, *The decay of OSL signals as stretched-exponential functions*, Radiation Measurements **37**, 519 (2004).

25. E. Bulur, *A simple transformation for converting CW-OSL curves to LM-OSL curves*, Radiation Measurements **32**, 141 (2000).

26. G. Blasse and B. Grabmaier, *Luminescent Materials*, Springer-Verlag, Berlin, 1994.

27. Q. Hu, L. Lei, X. Jian, Z. C. Feng, M. Tang, and D. He, Solid State Sciences **37**, 103 (2014).

28. M. Holston, J. McClory, N. Giles, and L. Halliburton, *Radiation-induced defects in LiAlO$_2$ crystals: Holes trapped by lithium vacancies and their role in thermoluminescence*, Journal of Luminescence **160**, 43 (2015).

29. A. Brant, D. Buchanan, J. McClory, P. Dowben, V. Adamiv, Y. Burak, and L. Halliburton, *EPR identification of defects responsible for thermoluminescence in Cu-doped lithium tetraborate (Li$_2$B$_4$O$_7$) crystals*, Journal of Luminescence **139**, 125 (2013).

30. W. Holton and T. Estle, *Electron paramagnetic resonance of photosensitive iron transition group impurities in ZnS and ZnO*, Physical Review **133**, 1638 (1964).

31. M. Auvray-Gely, A. Perez, and A. Dunlop, *Electron paramagnetic resonance and absorption studies of irradiated lithium aluminate*, Philosophical Magazine B **57**, 137 (1988).

32. A. Brant, D. Buchanan, J. McClory, V. Adamiv, Y. Burak, L. Halliburton, and N. Giles, *Photoluminescence from Ag^{2+} ions in lithium tetraborate (Li$_2$B$_4$O$_7$) crystals*, Journal of Luminescence **153**, 79 (2014).

33. D. A. Buchanan, *EPR and ENDOR Studies of Point Defects in Lithium Tetraborate Crystals*, PhD dissertation, Air Force Institute of Technology, Wright-Patterson AFB (2012).

REPORT DOCUMENTATION PAGE

1. REPORT DATE (DD–MM–YYYY)	2. REPORT TYPE	3. DATES COVERED (From — To)
26-03-2015	Master's Thesis	Sept 2013 — Mar 2015

4. TITLE AND SUBTITLE

Photoluminescence and Optically Stimulated Luminescence Studies of LiAlO$_2$ and LiGaO$_2$ Crystals

5a. CONTRACT NUMBER

5b. GRANT NUMBER

5c. PROGRAM ELEMENT NUMBER

6. AUTHOR(S)

Ferguson, Ian P., 2nd Lieutenant

5d. PROJECT NUMBER

5e. TASK NUMBER

5f. WORK UNIT NUMBER

7. PERFORMING ORGANIZATION NAME(S) AND ADDRESS(ES)

Air Force Institute of Technology
Graduate School of Engineering and Management (AFIT/EN)
2950 Hobson Way
WPAFB OH 45433-7765

8. PERFORMING ORGANIZATION REPORT NUMBER

AFIT-ENP-MS-15-M-106

9. SPONSORING / MONITORING AGENCY NAME(S) AND ADDRESS(ES)

Defense Threat Reduction Agency
ATTN: MAJ Thomas McQuary
8725 John J Kingman Rd Stop 6201
Fort Belvoir, VA 22060-6201
703-767-2500   thomas.mcquary@dtra.mil

10. SPONSOR/MONITOR'S ACRONYM(S)

DTRA

11. SPONSOR/MONITOR'S REPORT NUMBER(S)

12. DISTRIBUTION / AVAILABILITY STATEMENT

DISTRIBUTION STATEMENT A:
APPROVED FOR PUBLIC RELEASE; DISTRIBUTION UNLIMITED.

13. SUPPLEMENTARY NOTES

14. ABSTRACT

Copper diffusion in LiAlO$_2$ creates large photoluminescence (PL) and optically stimulated luminescence (OSL) signals that are not present in as-grown samples. The main PL band peaks at 3.45 eV (359 nm) and is excited by a band peaking at 4.54 eV (273 nm). After x-ray irradiation, OSL results from 425-500 nm continuous wave light. An optical absorption band in the same region decays during optical stimulation. Analysis of the wavelength dependence of the OSL emitted light reveals a band that is similar in peak location and width to the PL band suggesting that they occur at the same copper defect. The defects causing this optical behavior were identified using electron paramagnetic resonance (EPR) spectroscopy. During x-ray irradiation, Cu$^+$ ions trap holes to become Cu^{2+} ions while Fe^{2+} ions trap electrons to become Fe$^+$ ions. As a result of optical stimulation, released electrons recombine with holes at the Cu^{2+} ion sites. Copper diffusion in LiGaO$_2$ creates a large PL signal peaking at 2.33 eV (532 nm) that is excited by 3.50 eV (354 nm) light. This PL signal in LiGaO$_2$ is assigned to Cu$^+$ ions substituting for Li$^+$ ions.

15. SUBJECT TERMS

Luminescence, Optically Stimulated Luminescence, Lithium Aluminate (LiAlO$_2$), Lithium Gallate (LiGaO$_2$), Copper-diffused

16. SECURITY CLASSIFICATION OF:

a. REPORT	b. ABSTRACT	c. THIS PAGE
U	U	U

17. LIMITATION OF ABSTRACT

UU

18. NUMBER OF PAGES

69

19a. NAME OF RESPONSIBLE PERSON

Dr. Nancy C. Giles, AFIT/ENP

19b. TELEPHONE NUMBER (include area code)

(937) 255-3636, x4601; nancy.giles@afit.edu